AFWAL-TR-82-4026

DYNAMIC TENSILE TEST RESULTS FOR
SEVERAL METALS

UNIVERSITY OF DAYTON RESEARCH INSTITUTE
300 COLLEGE PARK DR.
DAYTON, OHIO 45469

APRIL 1982

DTIC
SELECTED
SEP 8 1982

H

INTERIM REPORT FOR PERIOD:
MARCH - SEPTEMBER 1981

APPROVED FOR PUBLIC RELEASE; DISTRIBUTION UNLIMITED

MATERIALS LABORATORY
AIR FORCE WRIGHT AERONAUTICAL LABORATORIES
AIR FORCE SYSTEMS COMMAND
WRIGHT-PATTERSON AIR FORCE BASE, OHIO 45433

82   034

NOTICE

When Government drawings, specifications, or other data are used for any purpose other than in connection with a definitely related Government procurement operation, the United States Government thereby incurs no responsibility nor any obligation whatsoever; and the fact that the government may have formulated, furnished, or in any way supplied the said drawings, specifications, or other data, is not to be regarded by implication or otherwise as in any manner licensing the holder or any other person or corporation, or conveying any rights or permission to manufacture use, or sell any patented invention that may in any way be related thereto.
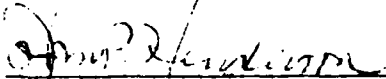
This report has been reviewed by the Office of Public Affairs (ASD/PA) and is releasable to the National Technical Information Service (NTIS). At NTIS, it will be available to the general public, including foreign nations.

This technical report has been reviewed and is approved for publication.

THEODORE NICHOLAS
Project Engineer
Metals Behavior Branch

FOR THE COMMANDER:

JOHN P. HENDERSON, Chief
Metals Behavior Branch
Metals and Ceramics Division

"If your address has changed, if you wish to be removed from our mailing list, or if the addressee is no longer employed by your organization please notify AFWAL/MLLN, W-PAFB, OH 45433 to help us maintain a current mailing list".

Copies of this report should not be returned unless return is required by security considerations, contractual obligations, or notice on a specific document.

REPORT DOCUMENTATION PAGE		READ INSTRUCTIONS BEFORE COMPLETING FORM
1. REPORT NUMBER AFWAL-TR-82-4026	2. GOVT ACCESSION NO. AD-A119054	3. RECIPIENT'S CATALOG NUMBER
4. TITLE (and Subtitle) Dynamic Tensile Test Results for Several Metals		5. TYPE OF REPORT & PERIOD COVERED Iterim Report March – September 1981
		6. PERFORMING ORG. REPORT NUMBER UDR-TR-82-05
7. AUTHOR(s) S. J. Bless, T. C. Challita, A. M. Rajendran		8. CONTRACT OR GRANT NUMBER(s) F33615-81-K-5082
9. PERFORMING ORGANIZATION NAME AND ADDRESS University of Dayton Research Institute 300 College Park Ave. Dayton, Ohio 45469		10. PROGRAM ELEMENT, PROJECT, TASK AREA & WORK UNIT NUMBERS 2422 05 02
11. CONTROLLING OFFICE NAME AND ADDRESS Materials Laboratory (AFWAL/MLLN) Air Force Wright Aeronautical Laboratories Wright-Patterson Air Force Base, OH 45433		12. REPORT DATE April 1982
		13. NUMBER OF PAGES 74
14. MONITORING AGENCY NAME & ADDRESS(if different from Controlling Office)		15. SECURITY CLASS. (of this report) Unclassified
		15a. DECLASSIFICATION/DOWNGRADING SCHEDULE

16. DISTRIBUTION STATEMENT (of this Report)

Approved for public release; distribution unlimited.

17. DISTRIBUTION STATEMENT (of the abstract entered in Block 20, if different from Report)

18. SUPPLEMENTARY NOTES

19. KEY WORDS (Continue on reverse side if necessary and identify by block number)

Impact Damage, Spall, Strength, Hopkinson Bar

20. ABSTRACT (Continue on reverse side if necessary and identify by block number)

Expanding ring and split Hopkinson bar experimental techniques were developed for study of dynamic yield behavior of metals. Preliminary results and spall data are presented for mild steel, armor steel, several aluminum alloys, OFHC copper, and nickel.

DD FORM 1473 1 JAN 73   EDITION OF 1 NOV 65 IS OBSOLETE

PREFACE

The work reported in this report was conducted under contract F33615-81-K-5082 for AFWAL/MLLN. The Contract Monitor was Dr. Theodore Nicholas. His many helpful comments during the execution of the program were greatly appreciated. Dr. Stephan Bless was the Principal Investigator for the University. Mr. Antonios Challita assisted with data analysis tasks. Dr. A. M. Rajendran assisted with the theoretical analysis of the behavior of aluminum. Stephan Hanchak was responsible for setting up the Hopkinson bar and expanding ring experiments. The experiments were conducted in the Impact Physics Laboratory at the University of Dayton.

Accession For

NTIS GRA&I ☑
DTIC TAB ☐
Unannounced ☐
Justification

By
Distribution/
Availability Codes
Dist | Avail and/or
      | Special

DTIC
COPY
INSPECTED
2

iii

TABLE OF CONTENTS

LIST OF ILLUSTRATIONS

List of Illustrations (Continued)

LIST OF TABLES

DEFINITIONS OF SYMBOLS AND ACRONYMS

A_b cross section area of bar

A_s cross section area of sample

BIM   beam intensity monitor, which measures the intensity of light reflected from the sample into the VISAR

C_b bulk wave speed ($\sqrt{K_s/\rho}$)

C_L longitudinal elastic wavespeed

d   flyer plate thickness

E   Young's modulus

F   void fraction on incipient spall surface

HEL   Hugoniot elastic limit (when yielding occurs in shock loading)

K   VISAR fringe constant, expressed as velocity increment causing one fringe

K_C critical value of K_λ for spall

K_S bulk modulus (incompressibility)

K_λ damage parameter in Tuler-Butcher equation

T   target thickness

x   distance measured along trajectory

x_s distance from incipient spall plane to target rear

Z   acoustic impedance

u   particle velocity

u_o impact velocity

U   shock propagation velocity

v   free surface velocity

v_s spall signal

Y   yield stress

Definitions of Symbols and Acronyms
(Continued)

r	radial coordinate
r_o	initial cylinder or ring radius
r_f	cylinder or ring radius at fracture
P	mean stress
ε	strain
ε_f	fracture strain
ρ	density
σ_1	largest principal stress
σ_o	threshold stress for void nucleation
σ_{min}	most tensile stress experienced by target
σ_r	radial stress component
σ_s	spall stress (stress at which spall occurs)
σ_{sp}	stress in sample
σ_θ	azimuthal stress component
γ	gas constant

SECTION 1

INTRODUCTION

Dynamic tensile yielding and fracture have been identified as priority areas for materials research.[1] The University of Dayton Research Institute has been active in this field for several years.[2,3] This interim report presents progress in material description and laboratory techniques during the period of March to September 1981.

The University research effort has focused on structural metals. Data are reported herein on 1020 steel, RHA (armor plate), several aluminum alloys, OFHC copper, and nickel 200.

The experiments have subjected the sample materials to various forms of dynamic tensile loading. Test geometries included flat plate impacts, expanding rings, and tensile Hopkinson bars. Some of the flat plate experiments were modified from those reported previously[3] by the addition of fused silica window discs. The expanding ring and Hopkinson bar test technique were wholly developed during the present reporting period.

This report presents tensile yield data for aluminum, mild steel, RHA, and copper. Tensile fracture data are presented for 1100 aluminum, RHA, and nickel. Developments in laboratory techniques are reported for every type of test.

SECTION 2
SPALL DAMAGE IN 1100 ALUMINUM

2.1 IMPACT EXPERIMENTS

Lower bounds for plate impacts that produce no damage in 1100 aluminum were not found in the previous effort.[3] Two plate impact tests were performed to obtain these limits.

The plate impact technique used previously[3] was modified slightly. Flyer plates had a step on their rear surfaces, so that each of the two halves was a different thickness. Nevertheless, regions of one-dimensional strain were produced in the target plate, in contrast to the wedge flyers plates used by some other investigators.[4]

A new tilt pin was also designed. Three insulated wires were inserted through holes in the target plates and lapped flush with the impact surface. They were positioned so as to be struck just inside the edge of the flyer plates. The place-ment and closure of these pins is considerably more precise than the self-shorting pins used previously. Tilt was less than could be resolved with the timing circuitry: 50 ns. In every shot, impact velocity, as measured between a barrel shorting pin and target contact, was in excellent agreement with streak camera records of the projectile taken just prior to impact.

The shots that were done, 376 and 383, employed d = 1 and 2 mm, and T = 4 mm at u_o = 211 and 234 m/s, respectively. Little damage was observed. An exceptionally clear VISAR record was obtained from shot 383, Figure 1. Unfortunately, the viewing area was near the center, so the release wave was not precisely one-dimensional. Two distinct arrivals are evident. In this shot the HEL is clearly defined at u = 20 m/s, corresponding to σ_1 = 3.6 kbar, or Y = 0.9 kbar.
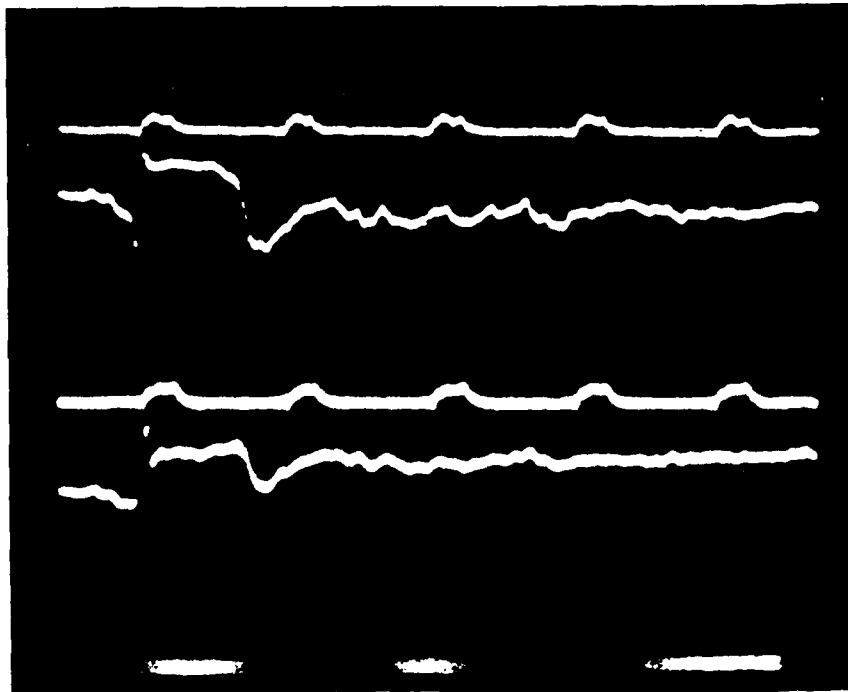
Figure 1. VISAR Record From Shot 383. Two quadrature channels.
Precursor and arrival of release wave are easily
distinguished. Time marks are 1 μs.

A new technique was developed for quantifying the spall
damage in targets. A cross-section through the damaged region
was prepared. The distance was measured from the center of
each void to the rear surface of the target for a significant
fraction of the void-filled region. Care was taken to avoid
regions of the target where the initial shock was not planar,
due to the finite diameter of the flyer plate. The mean of
these measurements was recorded. Next, an incipient fracture
line was drawn, through most of the voids, representing our
judgement of the path that the spall fracture would have
developed had the fracture been complete. Lastly, the percent-
age, F, of the incipient fracture line actually occupied by
voids was measured. These data are recorded in Table 1. Table
1 also includes data from Reference 3. Several previous inves-
tigations have defined spall separation as 50 percent failure
along the spall plane. This effectively corresponds to F = 50.

3

TABLE 1

SPALL OBSERVATIONS IN 1100 ALUMINUM

u (m/s)	d (mm)	T (mm)	Shot No.	Description	x_s (mm)	F (%)
211	1.0	4.0	376	no damage	--	0
234	1.0	4.0	383	no damage	--	0
300	1.0	4.0	272	connected voids	0.83±0.06	30
324	1.0	4.0	271	connected voids	NM	85
365	1.0	4.0	270	connected voids	0.79±0.05	70
472	1.0	5.0	51	cracks	0.80±0.11	75
590	1.0	5.0	50	voids	NM	NM
1556	1.0	5.0	52	voids	NM	NM
211	2.0	4.0	376	no damage	--	0
234	2.0	4.0	383	connected voids	NM	∿80
409	2.0	5.0	47	voids	--	--
570	2.0	5.0	49	connected voids	1.95±0.09	30
894	2.0	5.0	106	connected voids	NM	NM
1024	2.0	5.0	48	connected voids	NM	NM

There are some anomalies in Table 1 in which F is low for high velocity impact; this may be due to void closure. In only one shot, number 272, was the fracture less than complete. Many authors have suggested the concept of a critical void fracture, F_c, above which coalesence always occurs, followed by complete rupture. These results show $F_c > 30\%$.

2.2 SWAP CALCULATIONS FOR 1100 ALUMINUM

The SWAP code, as described in Reference 3, was modified to include the epoxy material behind the flyer plate. The effects of the epoxy were significant for aluminum flyer plates, although not for others. The residual stress at the flyer/epoxy interface after release was 9 kbar. This would have been zero, had the flyer been backed by air. A number of runs using various value of Y (yield stress) and σ_s (spall stress) were done for shot 272. Depending on the values of Y and σ_s input into the code, spall took place on either the

4

second elastic release wave or the leading plastic release wave reflected from the flyer rear surface. These cases are illustrated in Figures 2 and 3*. In Figure 2 spall occurs at x_s = 0.56 mm and in Figure 3 at x_s = 1.00 mm. Actually, spall occurs at x_s = ∿0.8 mm (see Table 1). Thus, SWAP is not capable of predicting the location of the spall plane.

It seems unlikely that any reasonable modification of the release wave profiles could affect this discrepancy. The spall signal must have originated after void initiation because it did not originate at the tail end of the release fan from the target rear surface. It is along this trailing characteristic that any specified level of tensile stress is first achieved. Thus, it appears that an incubation period was

SHOT 7-0272.PLOT3.AL/AL.U=300M/S.4/21/81
PSPALL= 8.PMIN=DMIN=0.05
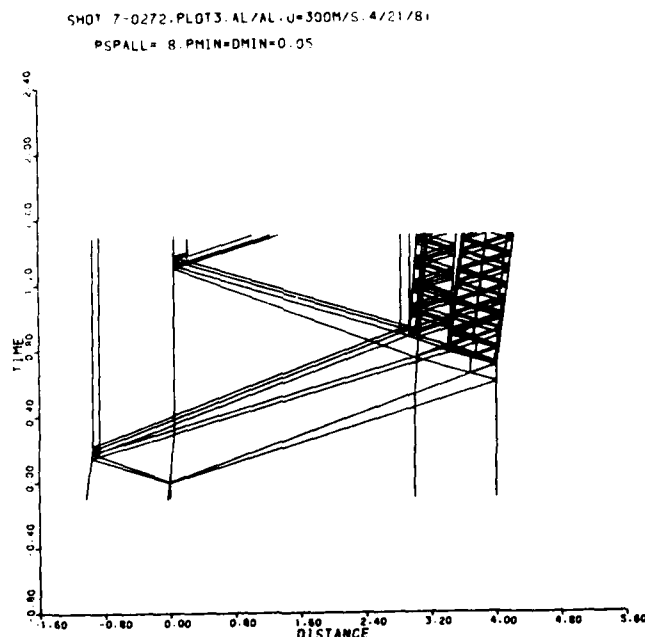
Figure 2. Characteristics Calculated by SWAP for Shot 272.
Y = 3 kbar, σ_s = 8 kbar. Impact is at x = 0,
t = 0. (Flyer is backed by air.)

---

* In these figures, as in other (x,t) diagrams presented in this report, impact occurs at this origin. The flyer plate moves from left to right. There is a reference line near the spall plane that does not represent a material interface.

5

SHOT 7-0272.EP-AL/AL.PLOTSA.Y=1.PS=7.SO.

U=300M/S.Y=1..12/28/81

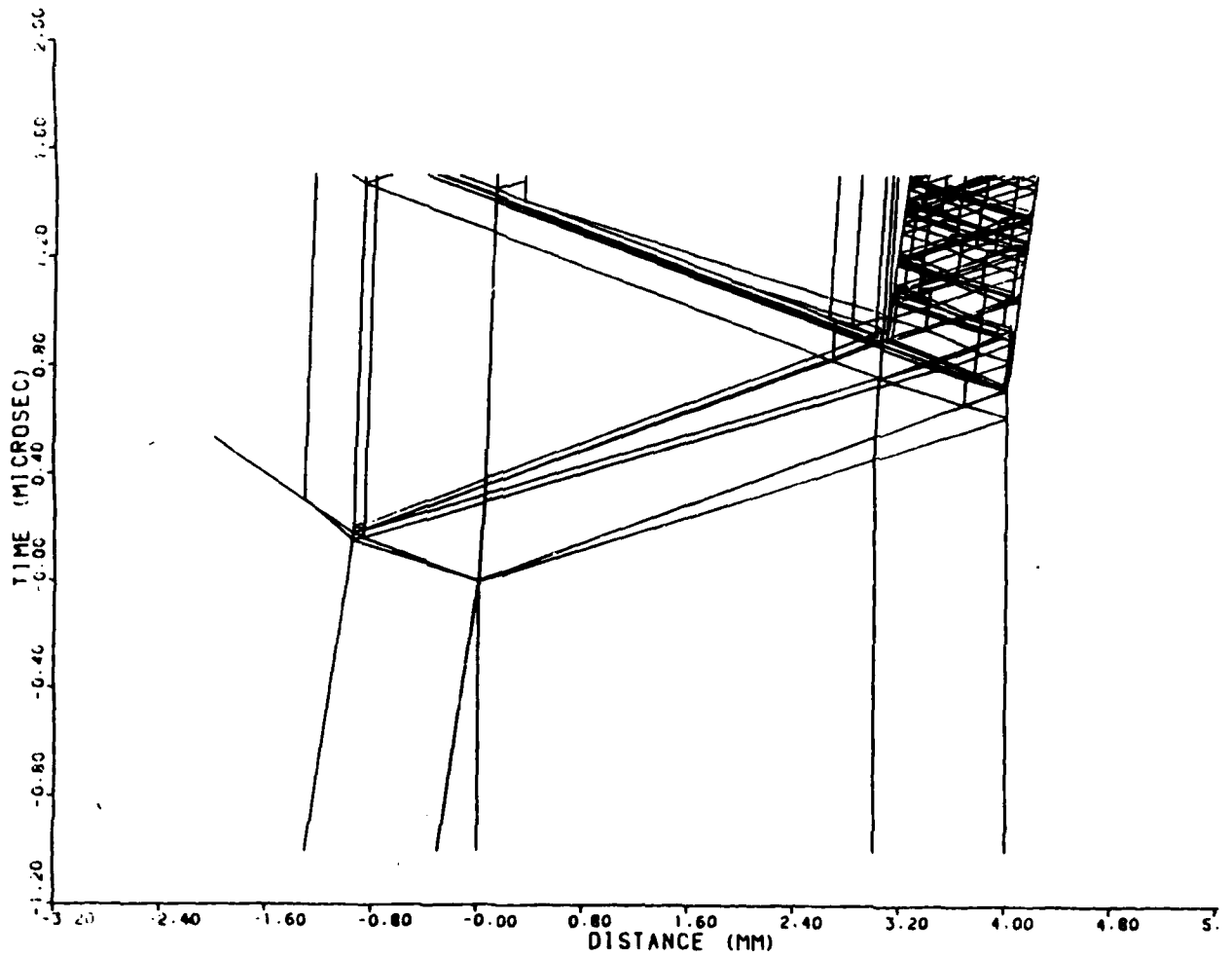Figure 3.   Characteristics Calculated by SWAP for Shot 272.   Y = 1.0 kbar, σ_s = 8 kbar.

necessary before the material "opened" on the spall plane,
generating the spall signal. Several different values of Y
were tried in order to match the observed free surface velocity
decay. Y = 1 kbar seemed to be best which is consistent
with the observations from shot 383. A free surface history
computed for shot 272 is shown in Figure 4. The free surface
history measured in the VISAR is shown in Figure 5 (the time
scale has been revised from Reference 3). These two velocity
histories still contain several descrepancies that are dif-
ficult to resolve. In the measurement, 0.25 μs elapsed
between the elastic precursor and shock arrival. In addition,
the precursor was not sharply rising. The precursor is much
more distinct in shot 383 (Figure 1), in which the precursor
arrival precedes the main shock by 0.21 μs. If we synchronize
the VISAR data and SWAP calculation by the arrival of the
plastic wave, then it is clear that the actual velocity decay
is more gradual than the predicted one. However, we are
not convinced that the VISAR data from shot 272 is an
accurate portrayal of the free surface velocity variation in
an aluminum target undergoing incipient spall. We intend to
perform several replications of the shot before attempting to
reach final conclusions. However, in general analysis of the
discrepancies between calculated and measured free surface
histories indicates that an elastic-plastic model, as is con-
ventionally used to describe release waves, and as is presently
used in SWAP, is incapable of reproducing the observed velocity
history and spall plane location. The release process is much
more gradual than is predicted by the model, in which two
rarefaction shocks of strength Y propagate throuch the shock
compressed material at the speed of longitudinal elastic waves.
In reality, all of the rarefaction waves seem to be dispersive.

In the SWAP calculations for shot 272, spall occurred
at σ_s = -12.0 kbar and did not occur at σ_s = -12.5 kbar. Thus,
the threshold spall stress for d = 1 mm is between -12 and
-12.5 kbar. Barker[5] has successfully modelled release profiles

SHOT 7-0272.EP-AL/AL.YO+1..
DEC 14, 1981

PS - 12
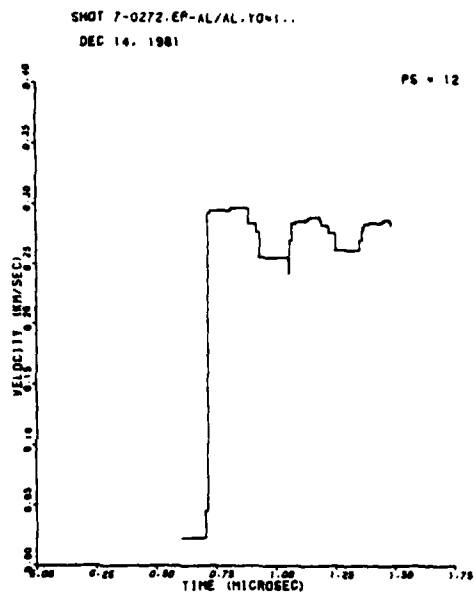
Figure 4.   Free Surface History Calculated by SWAP for Shot 272.
Y = 1 kbar, σ_s = 12 kbar.
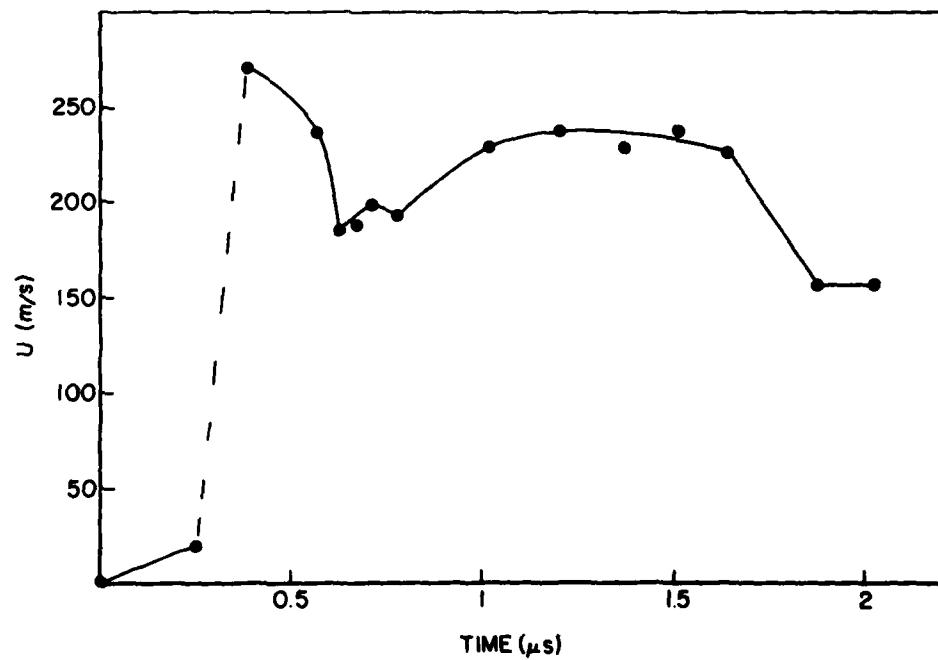
Figure 5.   Measured Free Surface Velocity for Shot 272.

8

such as Figures 2 and 5 using SWAP. He employed a yield stress that decreased during the release process. We have not tried that approach yet.

In order to correctly derive spall criteria, the complete release wave profile must be reasonably accurately calculated. However, in experiments such as these, only the leading characteristics of the release fan can be observed, because only they arrive at the target free surface undisturbed by the spall process. Thus, complete calibration of a SWAP model is not possible from these experiments. In order to obtain better release data, impedance-matching windows were placed on the target rear surface.

The revised target geometry is portrayed in Figure 6. The targets were backed with blocks of fused silica. Use of such a "window" material has been pioneered by researchers at

Figure 6.   Target Design Using Fused Silica Window.   (Dimensions in mm.)

9

Sandia Corporation (see Reference 6 for example). Fused silica has a shock impedance similar to aluminum. Hence, only a modest reflected tensile wave is produced when the impact-generated shock wave arrives at the metal/silica interface. Spall does not occur and the release waves propagating from the flyer plate rear surface are not significantly disturbed. However, the VISAR signal must be corrected for the effect of variations in the index of refraction of the silica window.
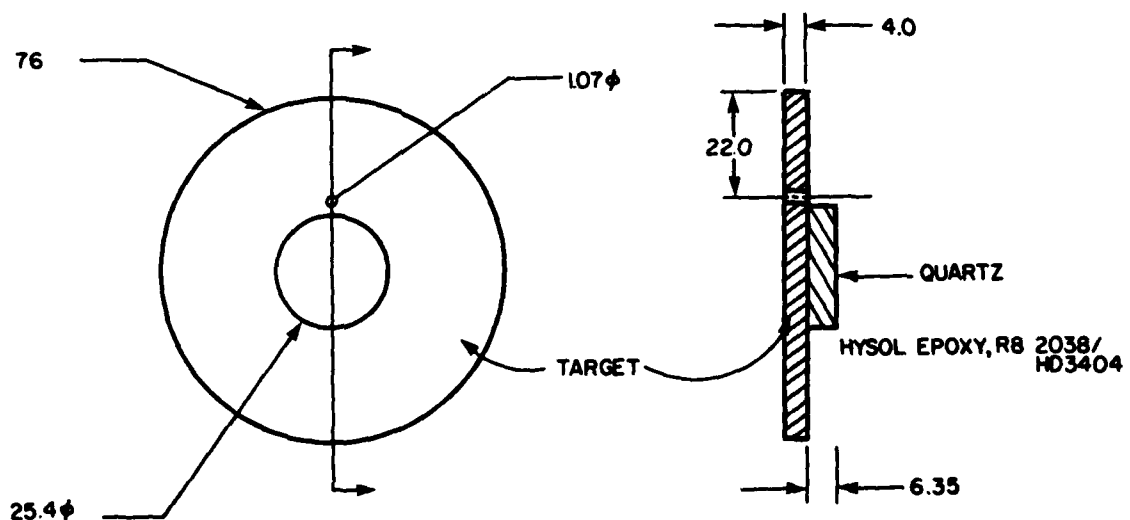
Reference 6 presents data for the dependence of index of refraction of silica on stress. Hence, in order to reduce the VISAR data, a SWAP calculation was run to determine the stress state in the silica as a function of time. The compression in the silica is always elastic, since Y = 98 kbar in this material. The loading data of reference 6 were used:

$$\sigma = 776\epsilon - 4159\epsilon^2 + 30340\epsilon^3 - 69260\epsilon^4 \tag{1}$$

(for σ in kbar). Equation (1) has the unusual property that there is a substantial stress range for which $\partial^2\sigma/\partial\epsilon^2 < 0$.

It turned out to be very difficult to run this model in SWAP, because SWAP assumes that elastic waves "shock up" and propagate at C_L. The release wave was also hard to model because $\partial K/\partial P < 0$ always led to code failure. Finally, it turned out to be practical to adjust the value of the shear modulus so that equation (1) was fulfilled.

The results of a sample calculation are shown in Figure 7. It is for an impact velocity u_o = 418 m/s. The peak stress was 33.2 kbar in the aluminum and 27.5 kbar in the silica. The anomalous behavior of the sound speed in silica can be seen by examining the evolution of the release waves emanating from the rear surface of the flyer plate. They spread in the aluminum, but shock up in the silica.

10

SHOT 7-0385.AL/AL-SIO2.PLOTIE.Y=98.NOC=5
NOK=0.POISSON=.173.S=0.01
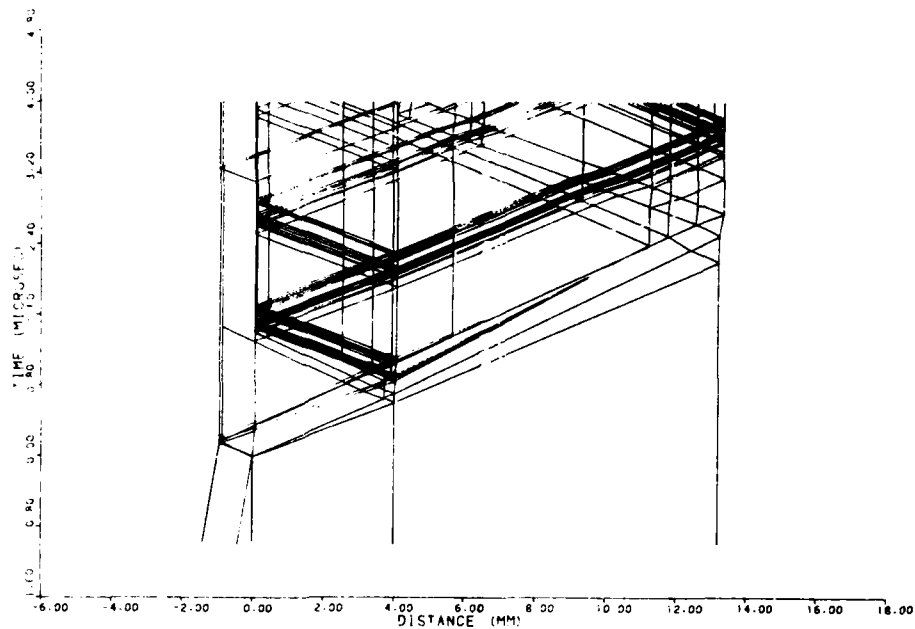
Figure 7. Characteristics in (x,t) Plane for Aluminum Target
Backed by SiO_2 Disc.

Eight shots have been conducted with silica windows.
Unfortunately, none have yielded fully satisfactory results.
The shots are listed in Table 2. No spall occurred in the
targets. In the first four tests, the VISAR was run with
glass etalons, for which the fringe constant was K = 338 m/s
fringe.

The first two tests were intended for practice and used
nickel targets. Polished silica windows were pressed directly
to the targets. The results were encouraging.

Following practice at Sandia[7], for subsequent targets
the silica front surface was depolished and aluminized. It
was bonded to the target with Hysol epoxy.

Of the aluminum targets, only shot 385 (Figure 8) yielded
good-looking data. However, the beam intensity record for this
shot was lost. (It was off-scale.) Some of the fluctuations

11

TABLE 2

SUMMARY OF SHOTS WITH SiO_2 WINDOWS

u (m/s)	d (mm)	T (mm)	Material	Shot No.	Results
576	2	5	Ni200	381	very noisy
580	2	5	Ni200	382	noisy, but reducible
432	1	4	1100Al	384	off scale
418	1	4	1100Al	385	noisy, but reducible
216	1	4	1100Al	483	HF noise
347	1	4	1100Al	485	HF noise, BIM off scale
343	1	4	2024Al	486	signals too small

of the signal in Figure 8 may be due to beam intensity varia-
tions, because it seems impossible to account for them with
a plausible interface velocity history.

In shot 483 the VISAR sensitivity was increased to
K = 51 m/s fringe in order to obtain more fringes and relieve
ambiguity in the data interpretation. The data were too noisy
to interpret. It also appeared that the data were affected
by light emission from the quartz. In shot 484 a gelation
filter was placed in the VISAR. However, there was still
excessive high amplitude high frequency noise. In shot 485
a narrow band interference filter was used. The BIM still
went off scale. The size of the beam stop for the reflection
from the silica rear surface was increased for shot 486.
Unfortunately, the resultant signal was of such low amplitude
that data reduction was not possible.

Experiments with silica windows will continue in the
next reporting period. Our approach will be to use higher
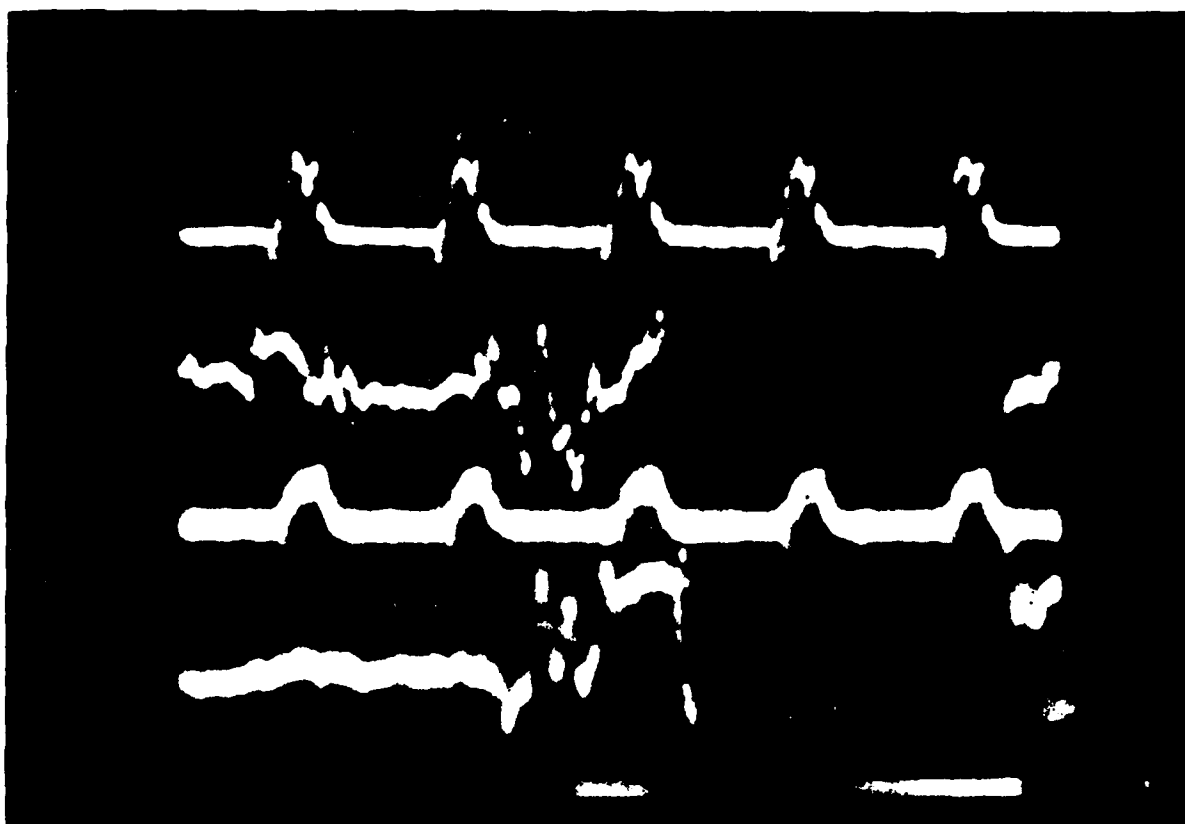recording speeds on the oscilloscopes and lower impact
velocities.

Figure 8. VISAR Data from Silica-backed Target; Shot 385. Time marks are 1 μs. Two quadrature signal channels shown.

SECTION 3
SPALL THRESHOLDS FOR RHA

3.1   IMPACT TESTS

The impact test data base reported in Reference 3 was
expanded in order to determine the dependence of spall stress
on tensile pulse duration. The total data set is presented
in Table 3. The stepped flyer plates and damage assessment
techniques described in the previous chapter were used for
many of the new shots.

Complete spall plate separation did not occur in the
stepped flyer plate experiments. This was apparently because
each half of the incipient spall plate could not separately
acquire sufficient momentum to rupture the unspalled material
around its periphery. However, in only one case was the damage
only partial--indicating that coalescence of voids and cracks
in RHA occurs very rapidly after their formation, and that
the critical void fraction for rupture is relatively small.

3.2   SWAP CALCULATIONS

The RHA impacts were modelled with the SWAP code. For
these calculations, the RHA Hugoniot from reference 8 was used:

$$U = 4.51 + 1.43 \, u. \tag{2}$$

A constant yield stress of 4.7 kbar was used, based on the
observed elastic precursor amplitudes.

For each shot, the most tensile stress, σ_{min}, was com-
puted at the spall plane location (spall being suppressed in
the code). The results are shown in Figure 9. It can be
seen that the data marginally support the assertion that more
tensile stress is required for fracture of the material when
the pulse length is relatively short. Spall may be approximately
characterized by a critical stress spall stress, σ_s, equal
to -52 kbar.

14

TABLE 3

SPALL THRESHOLD DATA FOR RHA

u_o (m/s)	d (mm)	T (mm)	Shot No.	Description	x_s (mm)	F (%)
391	0.5	4.0	379	no damage	--	0
283	1.0	4.0	371	no damage	--	0
319	1.0	4.0	372	isolated voids	1.17+0.13 1.63∓0.13	55
355	1.0	4.0	373	cracks	1.21+0.01	95
391	1.0	4.0	379	cracks	1.07+0.03	90
235	2.0	4.0	265	no damage	--	0
247	2.0	4.0	62	no damage	--	0
283	2.0	4.0	371	no damage	--	0
319	2.0	4.0	372	cracks	2.00+0.14 1.43∓0.15	90
355	2.0	4.0	373	cracks	2.31+0.03	95
380	2.0	5.0	60	spall	--	100
383	2.0	4.0	371	spall	--	100
390	2.0	4.0	268	spall	--	100
535	2.0	5.0	25	spall	--	100
771	2.0	4.0	21	spall	--	100

The Tuler-Butcher damage parameter, K_λ, was also calculated for the RHA impacts. The parameter is defined by

$$K_\lambda = \int (\sigma - \sigma_o)^\lambda \, dt \qquad (3)$$

$$|K_\lambda| > |K_C| \text{ for spall}$$

The model used to describe fracture in reference 9 assumed that voids initiate at -25 kbar. Therefore, calculations were executed with $\sigma_o \approx$ -20, -25, and -30 kbar in Equation (3).
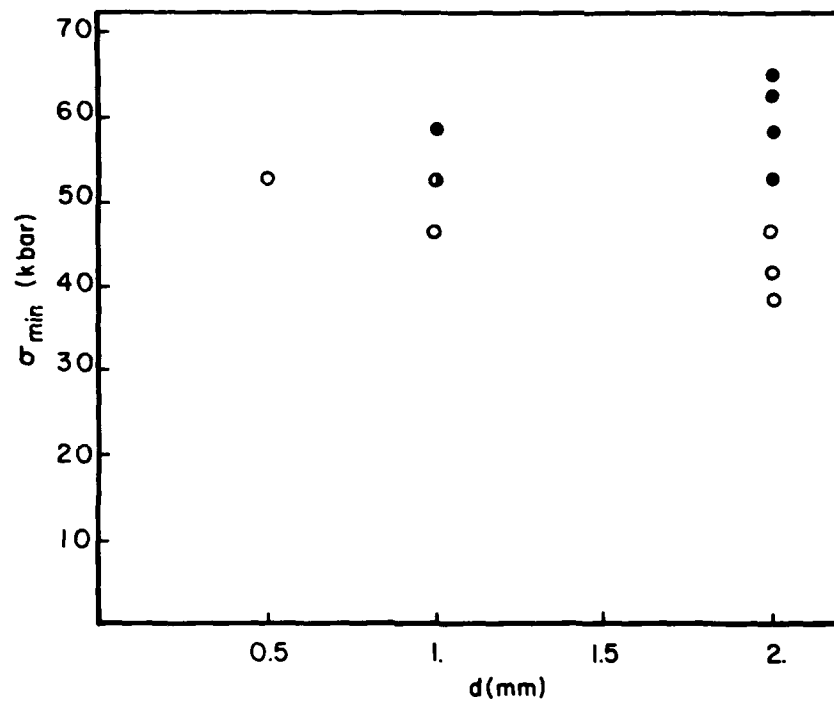
Figure 9. Effect of σ_s on d on Spall in RHA.
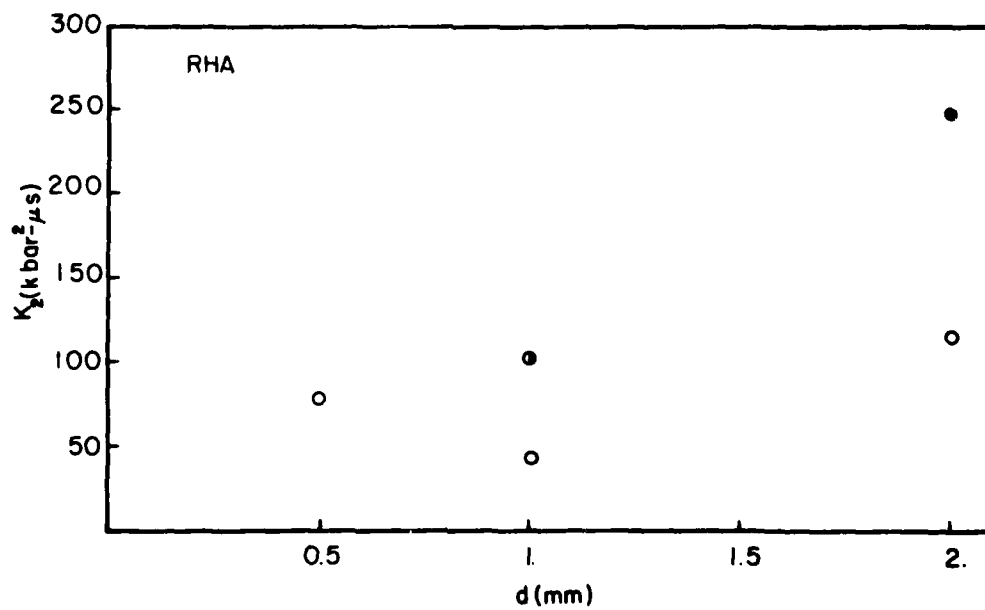
Figure 10. Effect of K_2 and d on Spall in RHA.

Both $\lambda = 1$ and $\lambda = 2$ were tried. Combinations were sought that would result in a value of K_C that does not depend on impact parameters. The best values were $\sigma_O = -30$ kbar and $\lambda = 2$, shown in Figure 10. $K_C = \sim 120$ kbar^2-s. However, this formula fits the data no better than the simple spall stress criterion with $\sigma_s = -55$ kbar. Therefore, over the loading range examined here, there is really no incentive to use a Tuler-Butcher time dependent criterion for this material.

SECTION 4

SPALL IN NICKEL AND COPPER

The data base established in Reference 3 for these materials has been expanded. As a consequence, the spall conditions are more precisely determined for these materials.

4.1 SPALL OBSERVED IN NICKEL

The material used here was nickel 200. This is a commercial pure alloy. The hardness of the targets was in the range of 67 to 75 on the Rockwell B scale (1/16-inch diameter ball, 100 kg load).

Table 4 shows the observations made on impacted targets. The table includes both new results and those from Reference 3. Figure 11 is a plot of maximum compressive stress (very nearly equal to σ_{min}) versus flyer plate thickness for Ni-200. SWAP calculations for this material have not been performed yet.

The data, as plotted in Figure 11, indicate a strong dependence of spall stress on load duration. However, these results must be interpreted with some caution because two different batches of nickel were used. All the specimens except shots 374 and 375 were from one batch, for which Figure 12 shows sample grain structure. Data from these two shots are flagged in Figure 11. Shots 274 and 275 used material (also supplied and certified as Ni-200) that had a slightly smaller grain structure (see Figure 13), although the same hardness, as the other material. However, the 274 and 275 material also contained inclusions (also shown in Figure 13). Failure seemed to initiate preferentially at the inclusions. In shot 274, although there was no preponderance of damage on the spall plane, there were several voids that had clearly initiated at inclusion sites. Consequently, the included material may be supposed to spall more easily. This explains why there is a more damage in shot 375 than shot 119.

18

TABLE 4

SPALL THRESHOLD DATA FOR NICKEL

| u (m/s)	d (mm)	T (mm)	Shot No.	Description	x_s (mm)	F (%)
278	0.5	5.0	380	Connected cracks	0.57±0.07	65
55	1.0	5.0	267	No voids	–	0
139	1.0	5.0	374	No voids	–	0
198	1.0	5.0	375	Voids	NM	80
205	1.0	5.0	119	Voids	1.01±0.05	45
278	1.0	5.0	380	Connected cracks	0.99±0.07	65
307	1.0	5.0	120	Spall separation	NM	NM
80	2.0	5.0	214	No voids	–	0
122	2.0	5.0	115	No voids	–	0
139	2.0	5.0	374	No voids	–	0
167	2.0	5.0	266	Voids	2.05±0.12	95
198	2.0	5.0	375	Voids	NM	80
229	2.0	5.0	116	Voids	2.14±0.10	90
236	2.0	5.0	218	Spall separation	NM	100
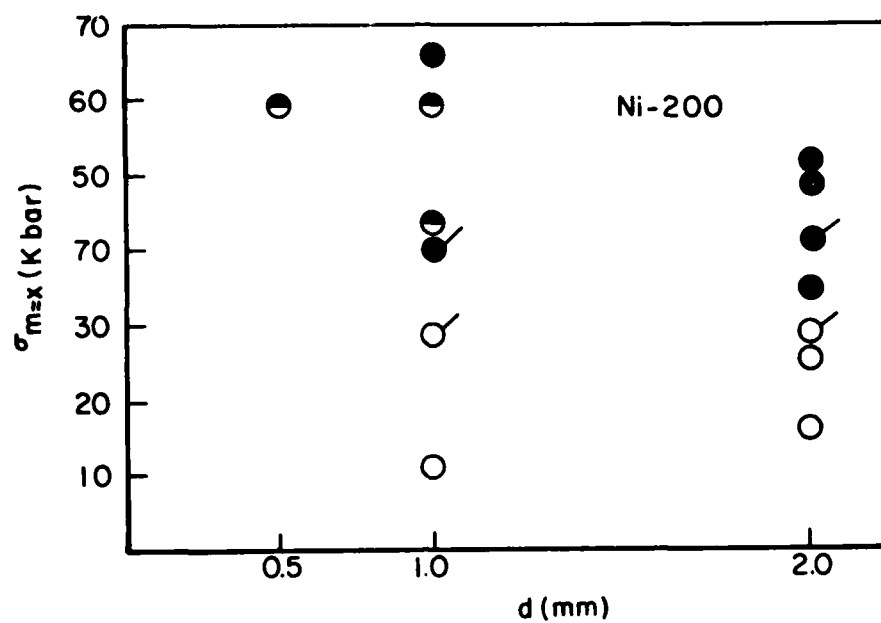
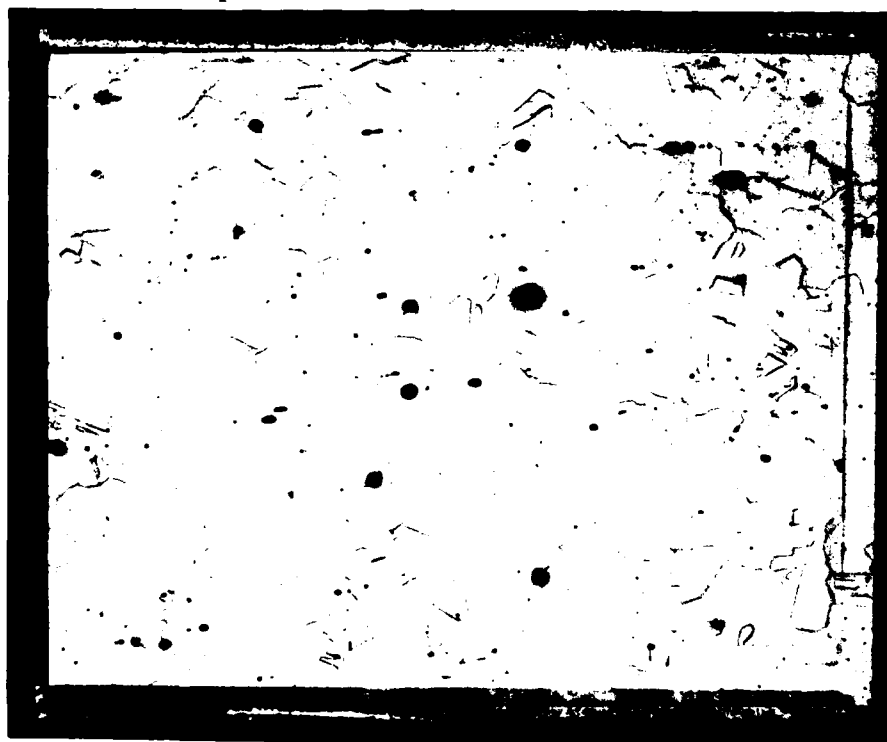Figure 11. Maximum Stress and Flyer Plate Thicknesses for Ni-200 Experiments.

Figure 12. Microstructure of Ni-200.

20

Consistent with this interpretation, we can confidently retain shot 274 as indicating impact conditions that do not result in spall in nickel 200.

Spall from thick flyer plates (d $\sim$ 2 mm) can be predicted by setting σ_s = -30 kbar. However, spall induced by thinner flyer plates will require a history dependent fracture model.

In shot 382 free surface release was measured for a nickel target backed by a fused quartz window (see Section 2). The VISAR trace was noisy, but an interpretation seemed feasible. An HEL of 5.6 kbar is observed, corresponding to Y = 6.6 kbar. This is consistent with Hopkinson bar measurements of tensile strength. On the one specimen tested, Y increased from an initial value of 2.5 kbar to 8.5 kbar at 20 percent strain.

Figure 13. Microstructure of Ni-200 Used in Shots 274 and 275, Showing Inclusion.

4.2 RESULTS FOR COPPER

The data reported in reference 3 showed the impact conditions resulting in incipient spall fracture in OFHC copper (approximately half-hard). However, there was an anomaly in the data, in that one shot (number 109) utilized an aluminum flyer plate. The results of that shot were not consistent with the other data obtained with copper flyer plates.

In order to resolve this conflict, shot 377 was conducted, utilizing an 1100 aluminum flyer plate with 1.5 mm and 2.0 mm steps. The results are shown in Table 5, together with the data of reference 3. The new results are much more consistent than shot 109. We conclude that shot 109 is fallacious; perhaps the velocity was incorrectly measured.

The most negative stress in shot 377 was -41 kbar, which is less than σ_s, according to reference 3 (Figure 20). The damage consisted of many closely spaced voids that would presumably would have formed a crack had a constant thickness flyer plate been used. Figure 14 shows K_2 for the data in Table 5 (without shot 109). It is evident that these results are consistent with $50 < K_{2C} < 110$ kbar^2 - μs, as concluded in reference 3. (See reference 3 for a discussion of the datum at d = 0.4 mm.)

TABLE 5

SPALL IN COPPER

| Velocity (m/s)	Max Stress (kbar)	Flyer Thickness (mm)	Target Thickness (mm)	Shot No.	Remarks
80	14	1.50	4.00	121	No voids
103	19	1.45	3.90	111	Void layer
244	45	1.45	4.00	110	Spall separation
366	41	1.50 Al	4.00	377	Void layer
168	30	2.0	4.00	221	Spall separation
189	35	2.0	4.00	220	Spall separation
322	35	3.0 (Al)	3.96	109	Void layer
366	41	2.0 (Al)	4.00	377	Void layer
286	53	2.5	3.94	108	Spall separation
334	62	2.5	4.00	222	Spall separation
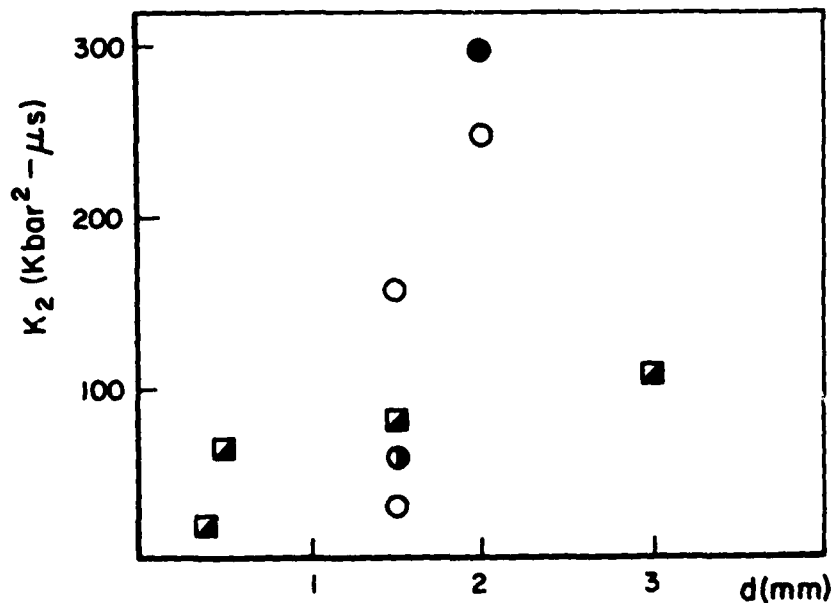
Figure 14. Damage Parameter K_2 for Spall in OFHC Copper.
(Squares are data from reference 10.)

23

SECTION 5
EXPANDING RING TESTS

5.1   BACKGROUND

Only a few test procedures are available for determination of constitutive relations at negative mean stress and high strain rates. The range around 10^4 s^{-1} is particularly difficult to achieve. Rapid mechanical machines are unable to achieve tensile stresses above 10^2 s^{-1}. The split Hopkinson bar tensile test (see next section) can extend this range another decade. Resolution of rapidly-changing stresses is difficult with a Hopkinson bar because of the effects of the sample grip on the transmitted waveforms.

Most studies of tensile failure at high strain rates utilize interaction of tensile waves produced from impact-generated shock waves, as in the spall work reported in preceding sections. These techniques are limited in that the subject material experiences intense compressive loading prior to tensile loading, and only states of one-dimensional strain are achieved.

The expanding ring technique presents an attractive supplement to conventional tensile test techniques. Relatively high rates can be achieved, $>10^4$ s^{-1}. Data analysis is free from complications involving wave propagation. Eventually, triaxial data may be obtained by testing rings with pre-drilled holes.

In the expanding ring test, an axially-symmetric thin short ring of material is driven radially outward. The ring may be launched explosively[11,12], with a magnetic field[13], with an exploding wire[14], or via a driver cylinder[15]. Most past work with expanding rings has been designed to measure ultimate strain at fracture. The ultimate strain is given by

24

$$\varepsilon_f = \ln r_f / r_o \qquad (4)$$

Where the average velocity, $\dot{r}$, is monitored, strain rate may be calculated from

$$\dot{\varepsilon} = \dot{r}/r \qquad (5)$$

Here r_o and r_f are, respectively, the initial radius of the cylinder and the radius at failure.

In the experiments of reference 15 as well as in those developed by the University, ring acceleration can be precisely measured. Before considering the experimental technique for generating the expansion, it is useful to consider the relationship between stress, strain, and ring motion. Analytical equations are evaluated with sample numerical values corresponding to a particular system of interest - a 20 mm diameter, 1 mm thick copper ring (density, ρ_o, of 8.82 g/cm^3).

The equations of equilibrium* for the expanding ring are:

$$\frac{\partial \sigma_r}{\partial r} + \frac{\sigma_r - \sigma_\theta}{r} = \rho \ddot{r} \qquad (6)$$

$$\frac{\partial \sigma_z}{\partial z} = 0 \qquad (7)$$

$$\frac{1}{r} \frac{\partial \sigma_\theta}{\partial \theta} = 0 \qquad (8)$$

and the boundary conditions are:

$$\sigma_r = 0 \text{ at outside surface}$$

$$\sigma_r = P \text{ at inside surface}$$

$$\sigma_z \sim 0$$

_____

*σ_r, σ_θ, and σ_z are respectively, stress in the radial, azimuthal and axial directions. P is the internal driving pressure.

In order to calculate σ_θ from $\ddot{r}$, it is necessary for P to be negligible. In that case, $\sigma_r = 0$, and a condition of uniaxial stress exists. The term $\partial\sigma_r/\partial r$ is of order P/h, where h is the instantaneous wall thickness. Since $h \ll r$, consideration of the first equilibrium equation leads to the requirement

$$P \ll \frac{\sigma_\theta h}{r} \qquad (9)$$

The above inequality imposes severe limitations on P. We expect $2 < \sigma_\theta < 4$ kbar. Take 3 kbar for illustrative purposes. The ratio h/r will be typically between 0.1 and 0.01. Lets take 0.05 as typical. Then we require that $P \ll 150$ bars. This condition is very difficult to achieve with explosives; the pressure of an expanding explosive may be estimated from:

$$P \text{ (in bars)} = (\frac{V_{gas}}{V_o})^\gamma \qquad (10)$$

where γ is the ratio of specific heats and V_{gas} is a property of the explosive and is equal to the volume which the detonation reaches in an adiabatic expansion to 1 bar. V_o is the STP specific volume of the detonation products. Typical values of V_o are ~ 600 cm^3/g, and a typical value for γ at low temperatures is 1.4. If the strain is 100 percent, and blowby is ignored, it turns out that P = 375 bars. This is several times higher than can be tolerated by the assumption σ_r is negligible. Thus, direct explosive driving of rings and cylinders is not an adequate technique for present purposes.

Most of the energy in the cylinder is kinetic. If a strain rate $\dot{\varepsilon}_j$ is to be obtained at a particular radius r_j, then the kinetic energy per unit length, T', is:

$$T' = \pi r_o r_j^2 h_o \rho_o \dot{\varepsilon}_j^2 \qquad (11)$$

For the ring in question at $\dot{\varepsilon} = 5 \times 10^4$ s^{-1} and $\varepsilon_j = \ln r_j/r_o = 1$, this equation gives 1.39×10^{10} ergs/cm. The strain energy in the cylinder at failure is approximately $Y\varepsilon_f$, where $Y =$ the yield stress. This is equal to 3.9×10^9 ergs/cm^3 for $\varepsilon_f = 1.3$ and $Y = 0.3$ kbar, or 1.23×10^9 ergs/cm of length. This energy is less than 10 percent of the kinetic energy. The important conclusions here are: (1) in order to achieve a given strain rate, the cylinder must be given a critical energy in an impulsive way; and (2) for strain rates of $>10^4$s^{-1}, failure will occur with a minimal decrease in kinetic energy.

The strain in the ring can be determined from the instantaneous diameter. The condition $P \sim 0$ permits the stress in the ring, σ_θ, to be determined by measuring the radial deceleration.

$$\sigma_\theta = -\rho r \ddot{r} \qquad (12)$$

If r is determined over intervals as $\Delta r/\Delta t$, then the uncertainty in $\ddot{r}$, $\delta \ddot{r}$, may be expressed as

$$\delta \ddot{r} = \{(\delta \Delta \dot{r}/\Delta t)^2 + (\Delta \dot{r} \delta \Delta t/\Delta t^2)^2\}^{1/2} \qquad (13)$$

As a numerical example, consider $\sigma_\theta = 3$ kbar and $\ddot{r} = 1.25 \times 10^8$ cm/s^2. If $\dot{r}$ is equal to one-half a fringe at maximum VISAR sensitivity, then $\Delta \dot{r} = 0.01$ mm/μs. The resolution should be 1/10 of this, so $\delta \Delta \dot{r}/\Delta \dot{r} = 0.1$. This occurs over $\Delta t = 8$ μs. The uncertainty in the time interval will be negligible. Thus, $\delta \ddot{r}/\ddot{r} \sim 10$ percent. Since there are two VISAR signals in quadrature, the net uncertainty will be close to 7 percent. The error in r is less than ~ 0.02 mm out of ~ 2.7 mm. Thus, the hoop stress, σ_θ, will be determined to better than 10 percent over ~ 10 μs intervals. The uncertainty will be less for longer times due to signal averaging.

5.2 EXPERIMENTAL TECHNIQUE

The technique used by the University for expanding rings uses an explosive charge inside of a cylindrical driver cylinder. After researching the availability of small explosive charges, it was found that significant cost and time savings could be achieved by using small charges already on hand. These were lead azide spheres, 10.8 mm diameter, of 1.7 g mass. They are centrally detonated by an embedded bridgewire.

An analysis was conducted to support the design of the expanding ring test. Equations were derived for the expansion of a cylinder driven by isentropic expansion of an explosively-generated gas. If the cylinder inner radius is r_o, and the charge is confined, the gas pressure is:

$$P = P_o (\frac{r}{r_o})^{-2\gamma} \qquad (19)$$

where P_o is the initial Chapman-Jouget pressure. Differential equations for cylinder motion were derived and numerically solved. A sample solution is shown in Figure 15, in which calculations are compared with data from reference 16. At least at early times, the agreement is satisfactory.

Seventeen explosive tests were conducted in order to develop the expanding ring technique. The first seven tests were dedicated to developing a driver cylinder that would undergo large radial expansion without fragmentation or gas leakage. The above analysis guided the design. Three materials were used: low density polyethylene, mild steel, and 6061-T6 aluminum.

The first two tests were conducted with polyethylene to determine the effect of cylinder length. The cylinders were 64 mm OD and 11.9 mm ID. 50 mm and 25 mm length tubes resulted in identical expansion, viz. 0.36 mm. All subsequent cylinders had a length of 50 mm. Test 6 utilized a smaller diameter
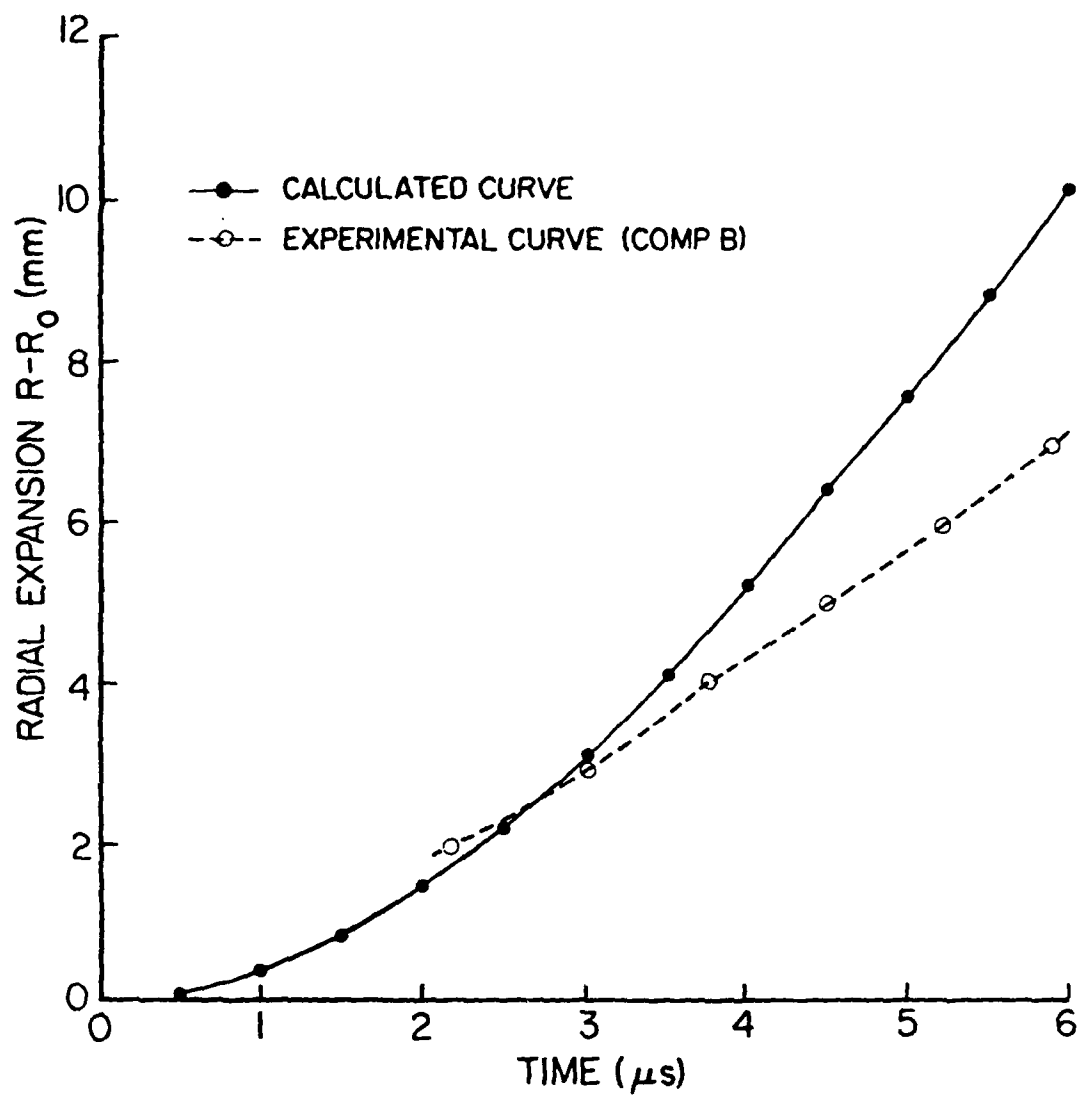
28

Figure 15. Expansion of Explosive Filled 25 mm Diameter Copper Cylinder.

polyethylene cylinder in order to increase the expansion. The
OD was 50 mm. The radial expansion more than doubled, but
was still only 0.86 mm.

Tests 3, 4, and 5 were with steel cylinders. The ID's
were 11.9 mm. The variation of expansion with OD can be seen
in Figure 16. The rapid increase in $\Delta r/r$ with decrease r led
us to believe that cylinder significantly smaller than 18 mm
diameter would rupture.

An aluminum cylinder was used in Test 7. It had an OD of
25.5 mm. Although the cylinder remained intact, radial cracks
were produced, and it was clear that even a very small reduction
in diameter would result in shatter.

The next stage in development of a ring test was to
demonstrate that rings could be launched in free expansion at
velocities of interest. For the developmental shots, it was
decided that a streak camera would be adequate for velocity
measurements. The camera employed was a Cordin Model 231,
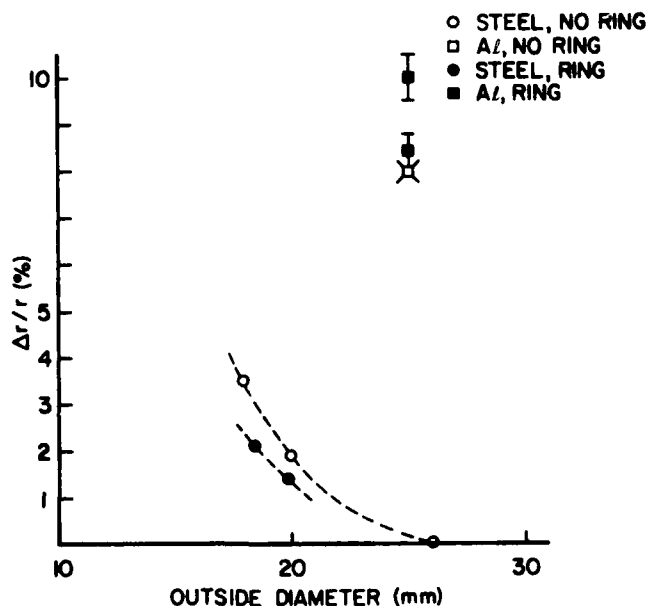which uses 70 mm wide film and is continuous access.

Figure 16.   Relative Growth in Driving Ring Diameters.   Cross
              indicates partial fracture.

Four shots were done to develop experimental techniques. The most difficult aspect was to assure prompt charge initiation, consistent with the limited recording time of the optical data train.

The system eventually developed is shown in Figure 17. A Vivitar flash unit was used for illumination. The flash duration was adjusted to be 600 µs. The flash had an unavoidable 200 µs pause in its trigger circuit. The camera was adjusted to run at between 0.5 and 1 mm/µs, so that the entire flash duration could be recorded without rewrite. The explosive had an unpredictable jitter of several hundred microseconds, even with steeply-rising high voltage initiation pulses. This jitter resulted in occasional loss of data. Figure 18 shows a sample streak record of a detonating charge. The initial expansion velocity is almost 7 mm/µs.

In shots 12 and 14 steel cylinders were employed to launch copper rings. The rings were cut from as-received OFHC copper tubing. In Shot 12, the driver cylinder OD was 18,0 mm and ID was 11.7 mm. A 1.9 mm thick ring was placed on the cylinder. The ring expanded in radius 0.62 mm, and the average logarithmic strain, from

$$\bar{\varepsilon} = \ln r_f/r_o \tag{15}$$

was 0.055 ± 0.005. For Shot 14 the ring thickness was reduced to 1.0 mm. However, the steel cylinder was a little larger, OD = 20.0 mm. The ring only expanded 0.45 mm, and the logarithmic strain was 0.040 ± 0.005.

In Shots 15 and 17 aluminum driver cylinders were evaluated. The shots were virtually identical; in Shot 15 the OD was 29.4 mm, and in Shot 17 it was 30.5 mm. Copper rings 1.96 mm thick were used. The average strains in these tests were 0.125 and 0.101, more than twice the best value obtained with steel cylinders. The aluminum was indented about 0.5 mm beneath the rings, which suggest that the acceleration was
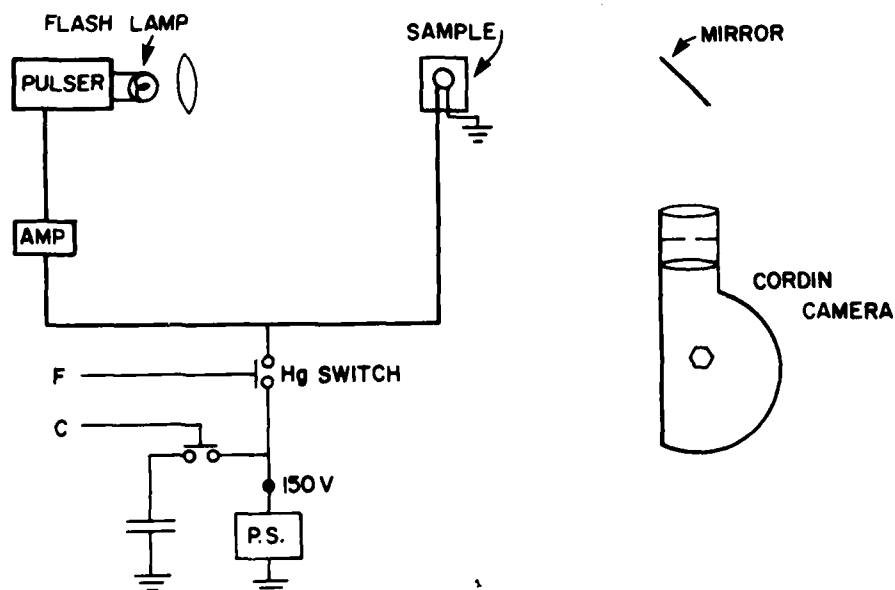
31

Figure 17.   Layout for Streak Camera Photographs of Expanding Rings.

Figure 18.   Streak Record of Detonating Charge.

gradual (since there was time for plastic flow around the ring).
Unfortunately, due to jitter in explosive detonation time, ring
velocity data were not obtained in either test. A curious
aspect of the tests was that the expansion of the aluminum
was greater than in Shot 7, even though there was no apparent
radial fracture. This is shown in Figure 16.

The final test was with a polyethylene driver cylinder.
The polyethylene OD was 50.5 mm. An aluminum ring was used of
unknown composition; its thickness was 3.0 mm. The average
strain was only 0.055 ± 0.003. Figure 19 shows the cylinder
after the test. It is apparent that the ring would have been
much more effectively launched were it thinner. The plastic
ruptured in one location behind the ring, releasing explosive
gases that would have invalidated a measurement of deceleration.

5.3   FURTHER DISCUSSION OF ALUMINUM DRIVER CYLINDERS

The aluminum driver cylinders used in Tests 15 and 16
appear to be strained to the fracture limit, based on the
following analysis. If $\varepsilon_z = 0$ and there is no net volume change,
$\varepsilon_\theta = -\varepsilon_r$. Near the surface, and probably through the cylinder,
$\varepsilon_\theta = \delta/r$, where δ is the displacement. The plastic strain is
$\varepsilon_p = \sqrt{2}\ \varepsilon_\theta = \sqrt{2}\ \delta/r$. For Test 15, this gives $\varepsilon_p = 0.14$.
The handbook value for maximum elongation for 6061-T6 aluminum
is 0.12. In a tensile test, $\varepsilon_z = \varepsilon_p$.

The maximum allowable ε_p in the cylinders will be less
than in a tensile test because P/Y is greater in the cylinder
test. To see this, consider that in the cylinder $\sigma_r = \sim 0$ and
$\sigma_z = a\sigma_\theta$ where $a < 1$. Hence, for the cylinder,

$$P/Y = \frac{1+a}{\sqrt{2}\,[1+2(1+a)^2]} \tag{16}$$

For $a < 1$ this is greater than 1/3, which is the value of P/Y
in a tensile test. Strain rate effects in this material are
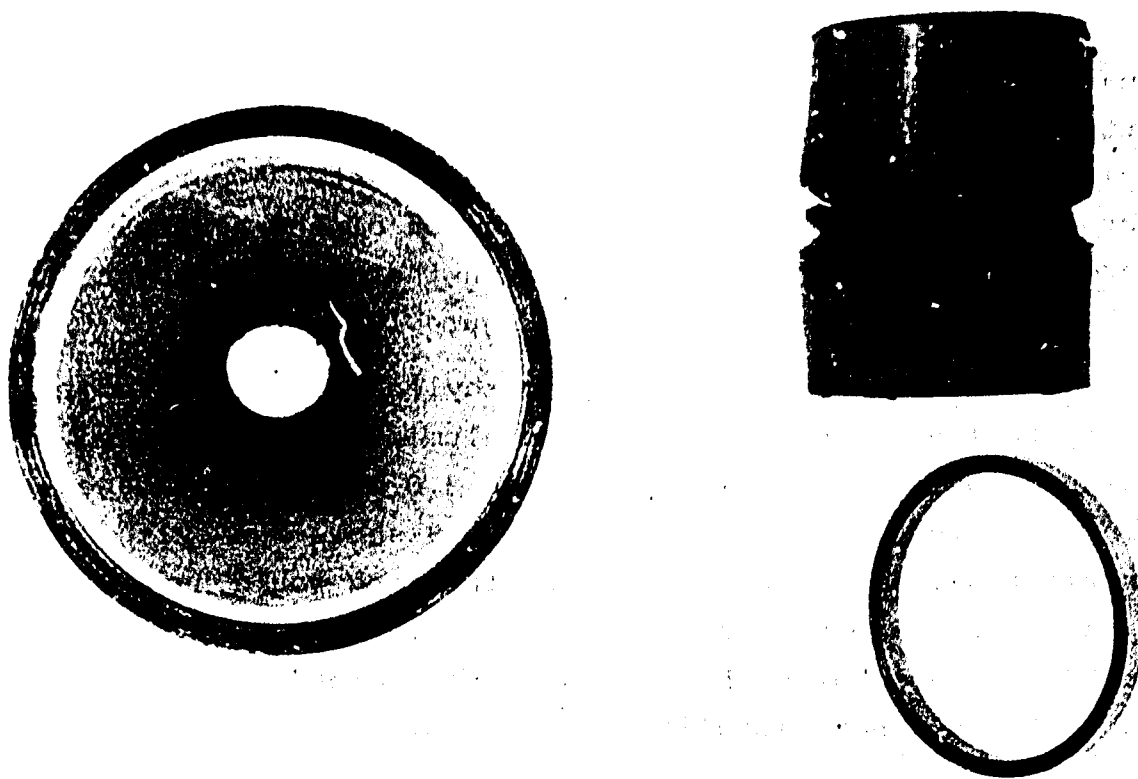
Figure 19.   Left: Top View of Polyethylene Driven Cylinder
             and Expanded Aluminum Ring.   Right: Side View.

not significant below about 2,000 s^{-1}, and it is unlikely that
strain rates are higher than that while plastic flow is taking
place.   Hence, it follows that the aluminum cylinders in Tests
15 and 17 could not have undergone significantly more expansion
without rupture.

Unfortunately, the launch velocity for the copper rings
driven by aluminum cylinders was not measured in these tests.
However, it may be estimated from the final diameter of the
rings and the assumption that the initial kinetic energy of the
ring was transformed into plastic work.

The plastic work per unit volume is approximately equal
to $1/2 \, \epsilon_p Y$.   The kinetic energy per unit volume is $1/2 \, \rho u_o^2$,
where u_o is the launch velocity.   Thus,

$$u_o \approx \sqrt{\epsilon_p Y / \rho} \qquad\qquad (17)$$

Substitution with $Y = 2$ kbar gives $u_o \sim 100$ m/s. The uncertainty in Y and the plastic work probably yields a 50 percent uncertainty in u_o. The strain rate is given by

$$\dot{\varepsilon} = u_o/r \qquad (18)$$

Thus, $\dot{\varepsilon}$ is in the range 0.4 to 1.2×10^4 s^{-1}. The upper end of this range is fully adequate for determination of useful yield strength data. However, larger values of $\dot{\varepsilon}$ are required if ultimate strain is to be determined.

Thinner copper rings may be launched at slightly higher velocities. If the time of arrest of the driver expansion was the same under the ring and away from the ring, then the potential gain in velocity by using thinner rings is simply the ratio of Δr alongside the ring and Δr directly under the ring. This ratio turns out to be 1.05. Thus, a very thin ring would be launched at about 5 percent higher velocity than the ring actually employed in Tests 15 and 17.

5.4 PLANS FOR FUTURE TESTS

Experiments were halted after Test 17 so that the results could be assessed and new cylinders fabricated. The following conclusions have been inferred from the results.

- Lower impedance drivers like aluminum and polyethylene are better than steel. They provide a more gentle launch of the ring because of plastic flow, and they are capable of imparting larger final strains to the ring. The preshocking of the ring noted by some other investigators may be avoided.

- The ring and driver configurations used in Test 15 and 17 are probably near optimum. The launch velocity should be determined to verify that the strain rate is at least 5,000 s^{-1}.

35

- More experiments should be done with polyethylene drivers using thinner rings. The objective should be to launch the rings at higher velocities.

SECTION 6

HOPKINSON BAR APPARATUS AND
RESULTS OF MEASUREMENTS

6.1   HOPKINSON BAR APPARATUS

The Hopkinson Bar apparatus used in this program is essentially identical to that described in reference 17. A number of minor mechanical modifications were carried out. The bars were realigned, which necessitated reworking the teflon bushing mounts, an oven was designed and fabricated, and new strain gauges were mounted. A high speed camera set-up was designed and deployed to photograph notched-tensile specimens under test.

The most substantial modifications of the bar from that described in reference 17 are in the way that data are recorded. Strain data from each strain gauge are now recorded directly on a digital oscilloscope. The sampling rate is usually 1 MHz. The gain is adjusted so that the signals of interest are captured with reasonable precision, even when this means that preceding wave arrivals are off scale. A computer program was written to analyze the strain gauge records. The program calculates strain, stress, strain rate, and stress versus strain.

The essential equations used to calculate specimen stress and strain have been described by many authors (for example, reference 17). A brief account is given here.

Strain gauges are placed equi-distant from the sample. The striker bar is launched against the pressure bar, producing a travelling compressive wave. In the present system, the duration is 300 μs. When the bar apparatus is used as a compression test, the initial compressive pulse is transmitted to the sample. The incoming pulse is partially transmitted through the sample, according to the relationship:

$$\sigma_{sp} = \frac{u_o A_b Z_b Z_s}{A_b Z_b + A_s Z_s} \tag{19}$$

where u_o is the striker impact velocity, A_b and A_s are the bar and sample cross section areas, and Z_b and Z_s are the bar and striker acoustic impedance (e.g., $\sigma_b = 1/2\, u_o Z_b$). The energy that is not transmitted to the specimen is reflected. Thus, very compliant or small samples ($A_s Z_s$ small) transmit little stress, and vice versa. The pressure bar/specimen interface acquires a velocity u_s ($u_s = \sigma_{sp}/Z_s$) which essentially imposes a boundary condition of approximately constant strain rate on the specimen. The stress in the specimen, σ_{sp}, is transmitted to the second, or transmission bar. The particle velocity imparted to the transmission bar is:

$$u_t = \frac{2\, u_s A_s Z_s}{A_s Z_s + A_t Z_t} \tag{20}$$

Since $A_t > A_s$, and usually $Z_t > Z_s$, this transmission is often quite weak. The reflected wave bounces back and forth in the sample, diminishing at each reflection from the transmission or pressure bar. The period is typically about 8 µs, so about 16 µs is required for the specimen to come to stress equilibrium with the Hopkinson bars.

When the bars are used for tensile tests, a collar is placed around the specimen. The collar supports the initial compressive stress. The transmitted wave reflects as a tensile wave at the end of the second bar. When the tensile wave returns to the specimen, the collar falls away, and the stress is sustained by the specimen. Figure 20 shows an (x,t) wave diagram for a tensile test. It is essential that the strain gauges be positioned so that the stress waves reflected and transmitted from the sample are recorded without interference from other waves.
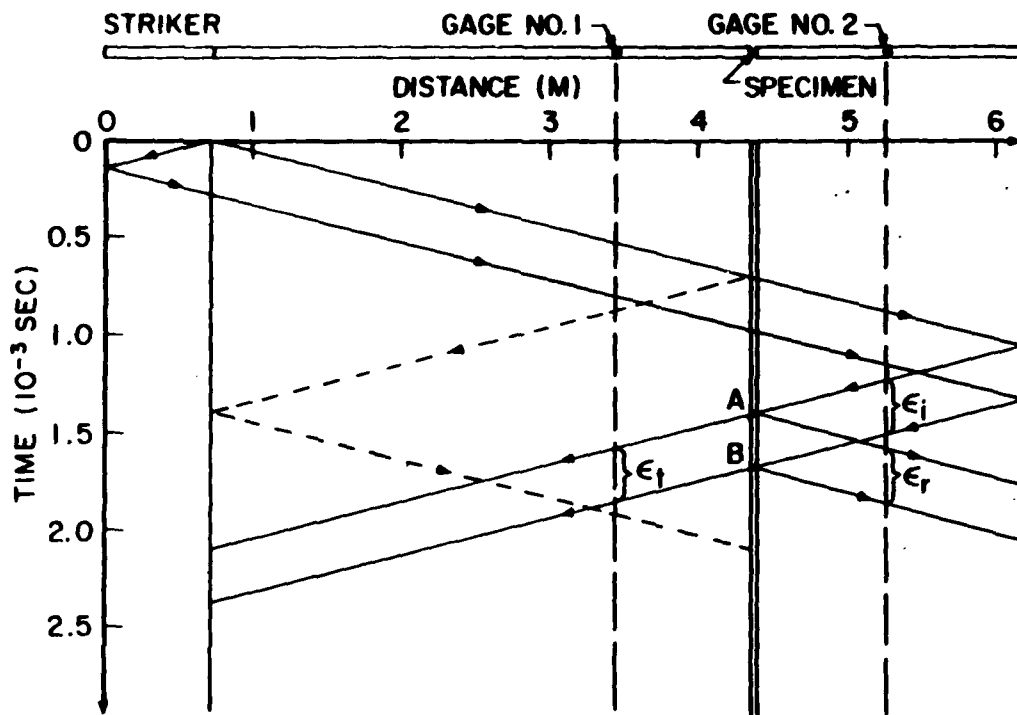
38

Figure 20.   (x,t) Diagram for Tensile Hopkinson Bar Test (from Reference 17).

The assumption that stress in the sample is uniform leads to the equation:

$$\varepsilon_s = \frac{-2c}{\ell} \int \varepsilon_r \, dt \qquad (21)$$

where c is the wave speed in the bar, ℓ is sample length, and ε_r and ε_s are reflected strain and specimen strain.   (Here, as elsewhere in this report, stress and strain are positive in compression.)   The specimen stress is given by:

$$\sigma_{sp} = E \frac{A_b}{A_s} \varepsilon_t \qquad (22)$$

when E and ε_t are the Young's modulus of the bar and the transmitted strain.   The specimen strain rate is given by:

39

$$\dot{\varepsilon} = - \frac{2c}{\ell} \varepsilon_r \qquad (23)$$

These equations show that the specimen strain is obtained by integrating the strain pulse reflected from the specimen, the specimen stress is proportional to the transmitted strain pulse, and the strain rate is proportional to the reflected strain pulse. The equations show that high strain rates are obtained by high striker velocities or short sample lengths. The equations are not valid for elastic response because equilibrium is not established during the time needed for the sample to "ring up" to the bar boundary conditions, as discussed above.

Equations (21) and (22) give average, or engineering, stress and strain. True stress and strain can be computed from:

$$\sigma_T = \sigma_{sp}(1 - \varepsilon_s) \qquad (24)$$

and

$$\varepsilon_T = \ell n(1 - \varepsilon_s) \qquad (25)$$

The bar strain gauges are easily calibrated by performing a compressive test with no specimen. Under those conditions, the strain in the bars is just

$$\varepsilon_b = u_o/2c \qquad (26)$$

Since the initial loading pulse is of duration τ (determined by the length and wave speed of the strike bar), the maximum strain that can be produced is

$$\varepsilon_{s,max} = \dot{\varepsilon}\tau \qquad (27)$$

For the bar used here, $\tau = 300$ µs.

The maximum allowable striker bar velocity is the velocity which causes the bar to deform plastically. For most

tests the bars were 1.27 mm diameter 4340 steel at RC 47. They
have a yield strength of Y = 14 kbar, which corresponds to a
maximum strain of $\epsilon_{b,max}$ = 0.007. It follows that $u_{o,max}$ =
71 m/s. In practice, the maximum velocity that can be achieved
is limited by the dimensions of the striker bar and striker
bar guide system to about 25 m/s. This means that for a stiff
sample, say of 4340 steel, the maximum strain rate is about
600 s^{-1}. In a very compliant sample, the maximum strain rate
is 2800 s^{-1}.

Figure 21 shows a photograph of the Hopkinson bar as set
up in the laboratory. Data that have been obtained with the bar
are presented and discussed in the following sections. Results
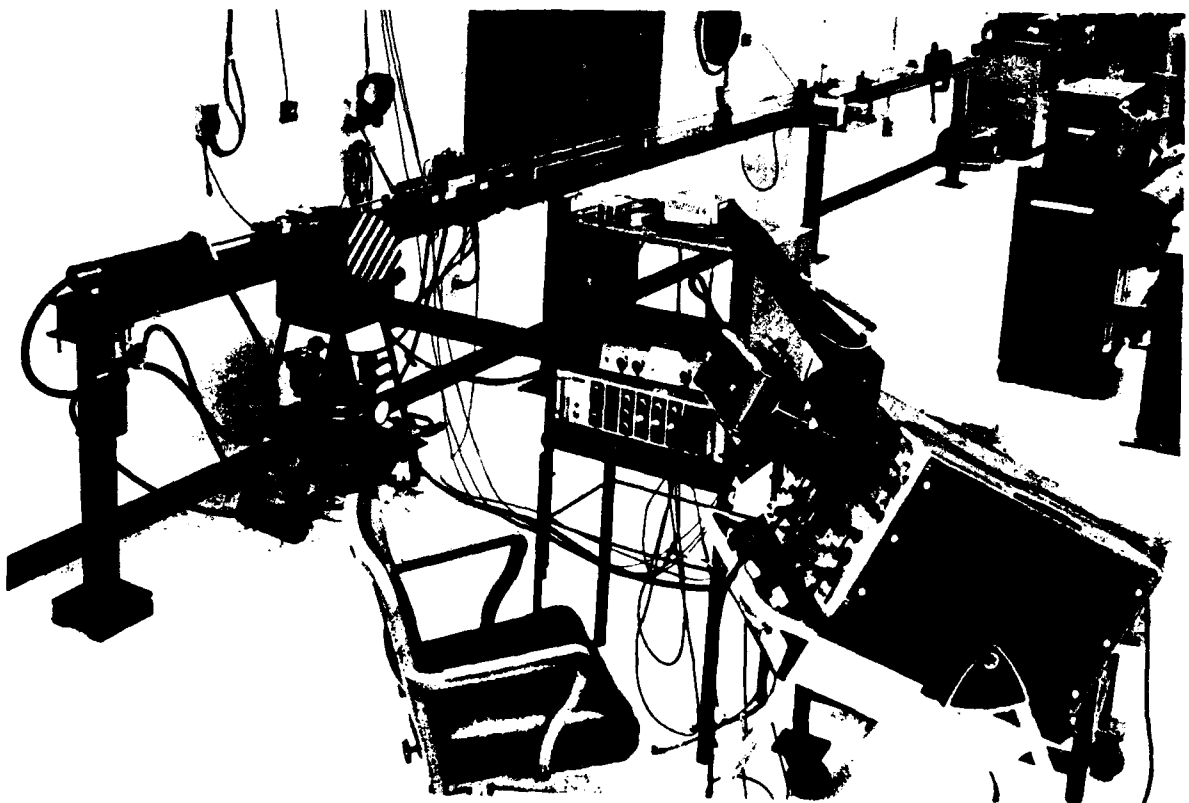have been very satisfactory with one exception. At higher

Figure 21. Photograph of Hopkinson Bar Apparatus.

launch velocities, the strain pulses are noisy. This becomes a problem for high strain rate studies (>1000 s^{-1}) of low impedance specimens (such as aluminum), for which the transmitted pulse is quite feeble and degraded by the bar noise. The noise is believed to be caused by flexural vibrations in the striker bar and ringing in the strain gauge amplifiers.

6.2   RESULTS OF HOPKINSON BAR TESTS

A summary of the tensile and compressive tests conducted are presented in Table 6. Seven different materials were tested in tension and one in compression.

6.2.1   Mild Steel

The 1020 steel samples were machined at the University and were tested in tension at strain rates ranging from 350 to 1,000 s^{-1}. A typical stress-strain plot from the digital data is presented in Figure 22. The stress-strain plots, for the various strain rates tested, were smoothed and are presented in Figure 23. The dotted line in Figure 22 represents a smoothed curve drawn to fit the data. Figure 23 clearly indicates a strain rate dependency for the 1020 steel. The yield stress increases with strain rate. Similar observations were reported in reference 18 for a mild steel tested in tension in a flywheel impact machine at 70°F. The "overshoot" often observed in mild steel at the beginning of the stress-strain curve (reference 17) could not be distinguished from the digital stress-strain plots, possibly because of the superimposed oscillations at the beginning of the signal attributed to the wave propagation mechanism in a long bar. For the same reason, an accurate yield stress can not be measured; an average yield stress was estimated and reported in column five of Table 6.

6.2.2   Aluminum 1100 Alloy

Five 1100-0 Al specimens were machined and tested in tension at the University. The stress-strain curves from
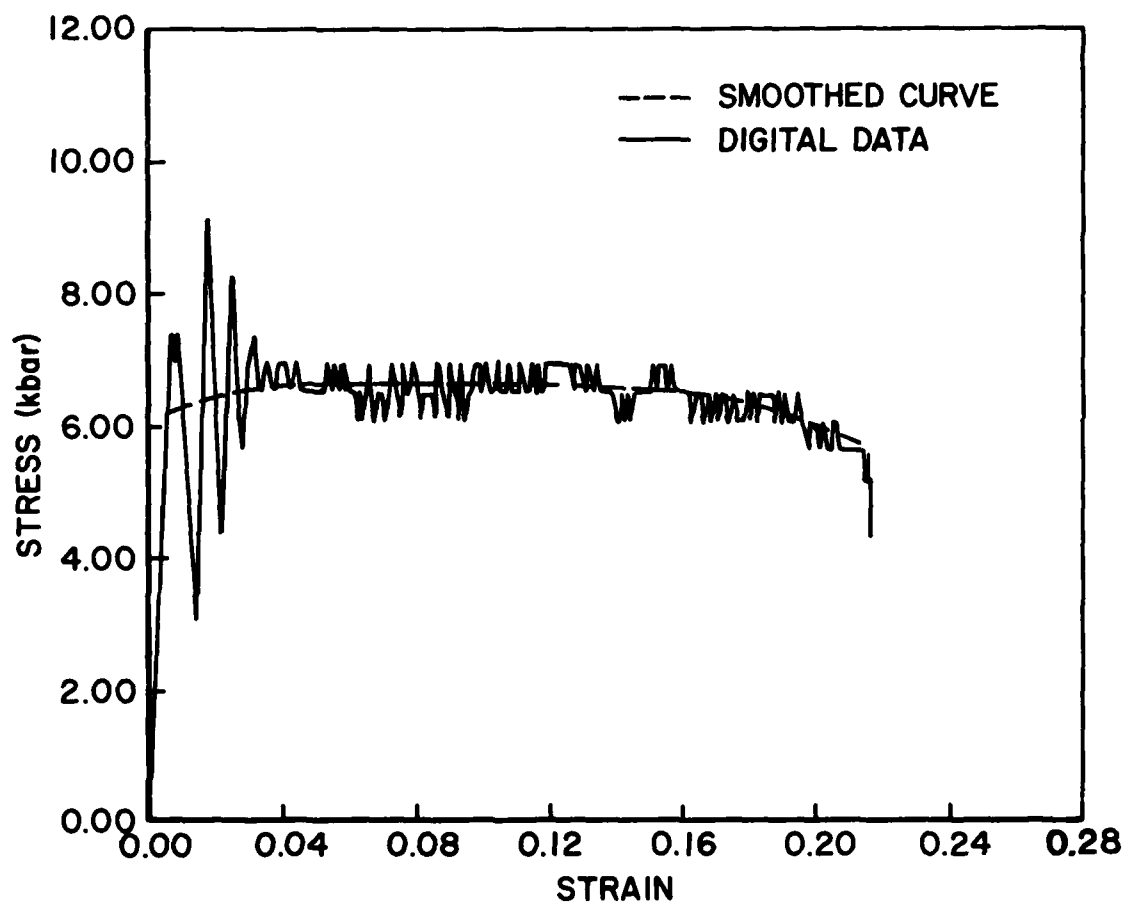
42

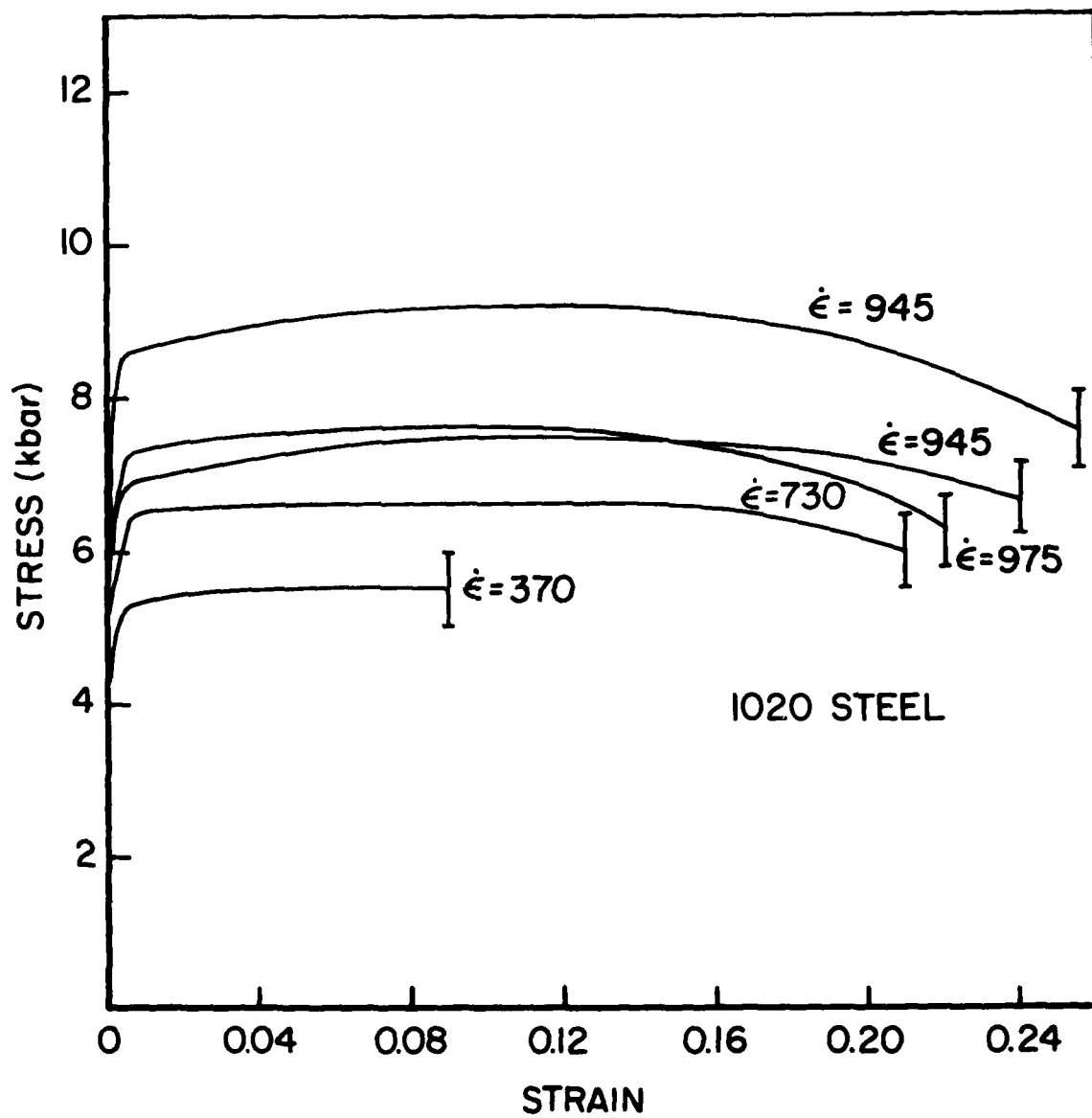Figure 22. Measured Stress-strain Curve for a 1020 Steel
Specimen (Shot 24).

Figure 23. Averaged Stress-strain Behavior for 1020 Steel at
Various Strain Rates.

44

TABLE 6

SUMMARY OF TESTS AND RESULTS

Shot #	Test Type	Material and Supplier	Strain Rate (1/s)	Yield Stress (kbar)	True Yield Stress (kbar)
HB016	Tension	1020 Steel	370	5.5±0.45	
HB024	"	(UD)	730	6.6±0.4	
HB026	"	"	945	7.2±0.5	
HB027	"	"	945	9.1±0.47	
HB029	"	"	975	7.3±0.4	
HB032	"	1100 Al	1215	1.8±0.45	
HB033	"	(UD)	1200	2.65±0.45	
HB034	"	"	890	1.75±0.42	
HB036	"	"	870	1.96±0.5	
HB037	"	"	550	1.85±0.4	
HB040	"	Al (3003)	330	1.95±0.2	
HB041	"	"	340	2.37±0.2	
HB043	"	"	185	1.94±0.1	
HB044	"	"	555	2.06±0.25	
HB059	"	"	525	3.12±0.5	
HB060	"	"	650	2.95±0.2	
HB064	"	"	1450	2.68±0.2	
HB066	"	"	360	2.0±0.1	
HB047	"	2024-T4 Al	280	4.3±0.3	
HB048	"	(Eglin)	475	4.5±0.3	
HB049	"	"	480	4.4±0.3	
HB050*	"	"	800	5.1±0.3	
HB051	"	OFHC Copper	545	2.01±0.22	
HB052	"	(Eglin)	525	2.5±0.3	
HB053	"	"	355	2.45±0.2	
HB054	"	"	860	2.45±0.4	
HB045	"	OFHC Copper (UD)	750	4.65±0.25	
HB056	"	Nickel 200 (UD)	770	3.42±0.22	
HB069	Compression	Al (3003)	2900	3.34±0.07	3.02
HB070	"	"	2875	3.6±0.07	3.2
HB071	"	"	2780	3.3±0.07	2.98

* The observed strain at which the specimen failed was 0.21.

these tests indicate that the yield stress is slightly sensitive
to the strain rate, for the range tested between 550 and 1210 s^{-1}
(see Figure 24). The relatively large uncertainty in the yield
stress values evident in figure 24 is a result of the low gain
setting of the oscilloscope during the testing. These results
agree with the work reported in references 19 and 20, who found
that high purity aluminum is highly strain-rate sensitive, while
aluminum alloys are insensitive over the same range of strain
rates.

6.2.3   Aluminum 3003 Alloy

Several 3003 aluminum specimens were supplied by
BRL. These were tested at the University in tension and
compression. Tests were conducted at various strain-rate
levels using the split Hopkinson Bar technique. Tests were
also conducted under quasi-static loading conditions so that
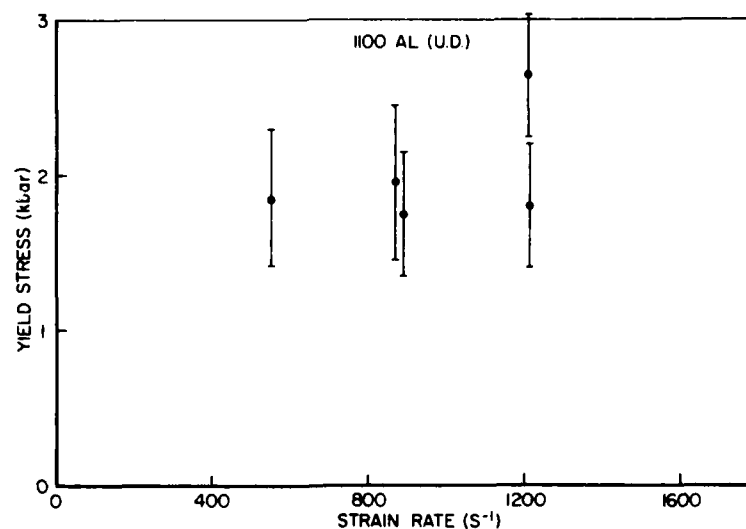
Figure 24.   Yield Stress Measured for 1100 Aluminum.

the low strain-rate behavior of the material could be compared
to the dynamic behavior.

Data from individual stress-strain tests have
been averaged in order to obtain the characteristic behavior
at various strain rates. The average results are shown in
Figure 25. The strain-rate dependency of the material is
clearly evident. Considerable increase in the value of dynamic
flow stress occurs even at intermediate strain-rate levels
(500 to 600 s^{-1}). The strain-rate sensitivity of the material
seems to be decreasing with the increasing strain-rate beyond
this level. Within the scatter in the data, the maximum flow
stress for a strain-rate of 1400/s does not differ from the
value at intermediate strain-rate levels. This may mean that
variation of flow stress with strain-rate is not significant
for $\dot{\varepsilon} > {\sim}500$ s^{-1}.
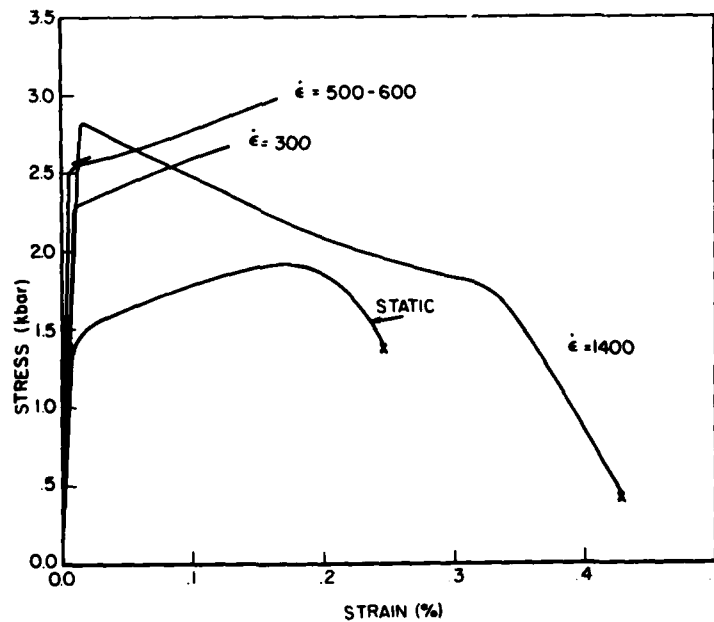
Figure 25. Average Stress-strain Behavior of 3003-aluminum at
Various Strain Rates.

It is also interesting to observe at a strain-rate level of 1400 s^{-1}, the flow stress reaches maximum at the initial yield, and then decreases. This can be interpreted as analogous to the strain softening which occurs at point-of load maximum in a static test. At high strain rates, the elongation is quite considerable beyond the initial plastic instability point. This confirms the theoretical result, reported by Hutchinson and Neale[21], that there is an increase in the post-uniform elongation due to an increase in strain-rate sensitivity (m) of the material.

Figure 26 is a schematic representation of the data in Figure 25, in which two types of instabilities are illustrated. While the first-instability point (A) corresponds to the load maximum point, the second instability point (B) corresponds to localized necking. The theoretical results indicate that the first point of plastic instability occurs at lower values of the uniform strain for increasing strain-rate levels[22,23]. Figure 25 is in agreement with this prediction. In the limiting case, the point (A) occurs before any strain hardening takes place, as shown by the 1400 s^{-1} cruve.

The deformation process beyond the load maximum point (A) is quasi-stable and the amount of uniform straining depends on the strain-rate dependency of the material. Several investigators have reported that ductility in rate sensitive materials decreases as strain rate increases. These predictions were experimentally confirmed by Sagat and Tapling[24] for quasi-static loading. However, under dynamic loading conditions observed here, ductility increased with strain-rate level. This means that the inertia of the deformation process post-phones the occurence of localized necking which precipitates the instability (B) in Figure 26. The test results on 3003-aluminum are also agreement with the observation of additional ductility in copper and 6061 aluminum at high strain rates[11,19].
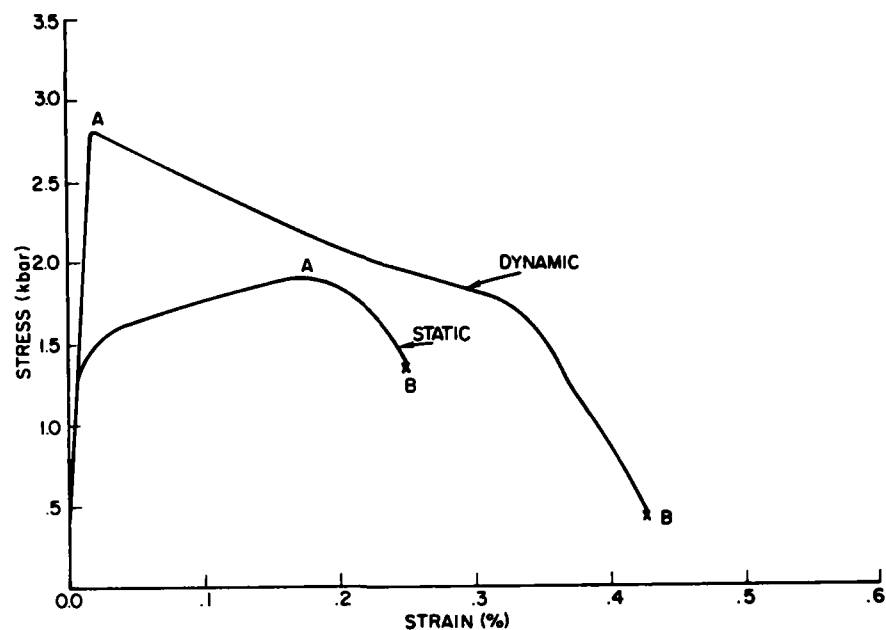
Figure 26. Low Strain Rate and High Strain Rate Behavior, Illustrating Instabilities.

In one of the tests, the sample was dynamically strained without failure to an uniform strain of 11.5 percent. The maximum strain rate in this test was 200 s^{-1}. The dynamically pre-strained sample was then statically loaded to failure as shown in Figure 27. The static portion of the stress-strain curve of this sample apparently follows the same static stress-strain curve as samples without any dynamic pre-strain. It can be concluded that the material behavior is independent of past history (dynamically loaded and then unlaoded). Similar behavior was observed in aluminum 6061-T4 and Al 6061-T6[14]. These are relatively strain-rate independent materials, whereas the present results were obtained for a rate-dependent material.

In contrast to Figure 27, the test results of Fyfe and Rajendran[14] for a strain-rate dependent-material, namely, annealed copper indicate that plastic flow behavior upon
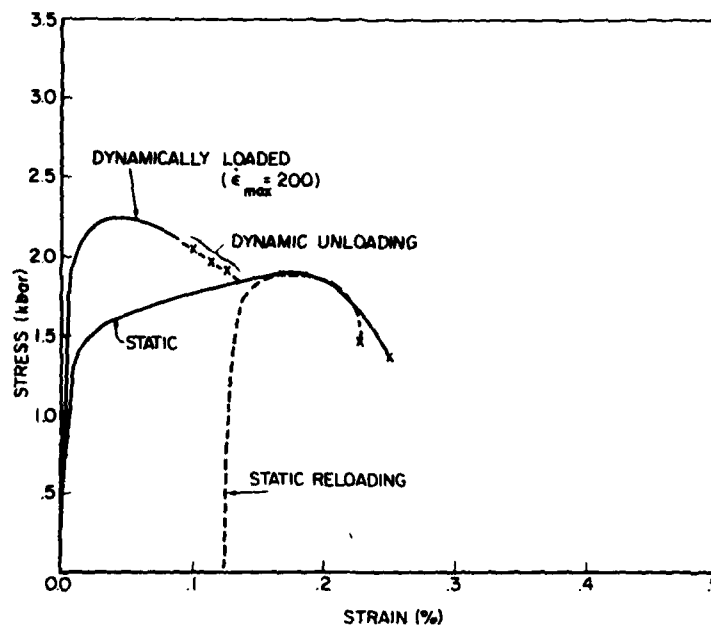
49

Figure 27. Comparison of Dynamic, Static, and Dynamic-Prestrained Behavior of 3003-aluminum.

static reloading on dynamically prestrained thin cylinders does depend on the past dynamic loading; the material is strain-rate hardened due to the dynamic loading. The static stress-strain curve of the dynamically restrained sample remains higher than the static stress-strain curve of the sample without any prior history.

Three 3003 Al specimens were tested in compression at a strain-rate of 2850 s^{-1}. The records from one of the compression tests are presented in Figure 28. True stress and true strain data were calculated for these tests as well. The true stress-true strain curves show an upper and lower yield points and a relatively constant flow stress (see Figure 29). The upper yield, lower yield, and the flow stresses were 3.0, 1.85, and 2.3 kbars, respectively.
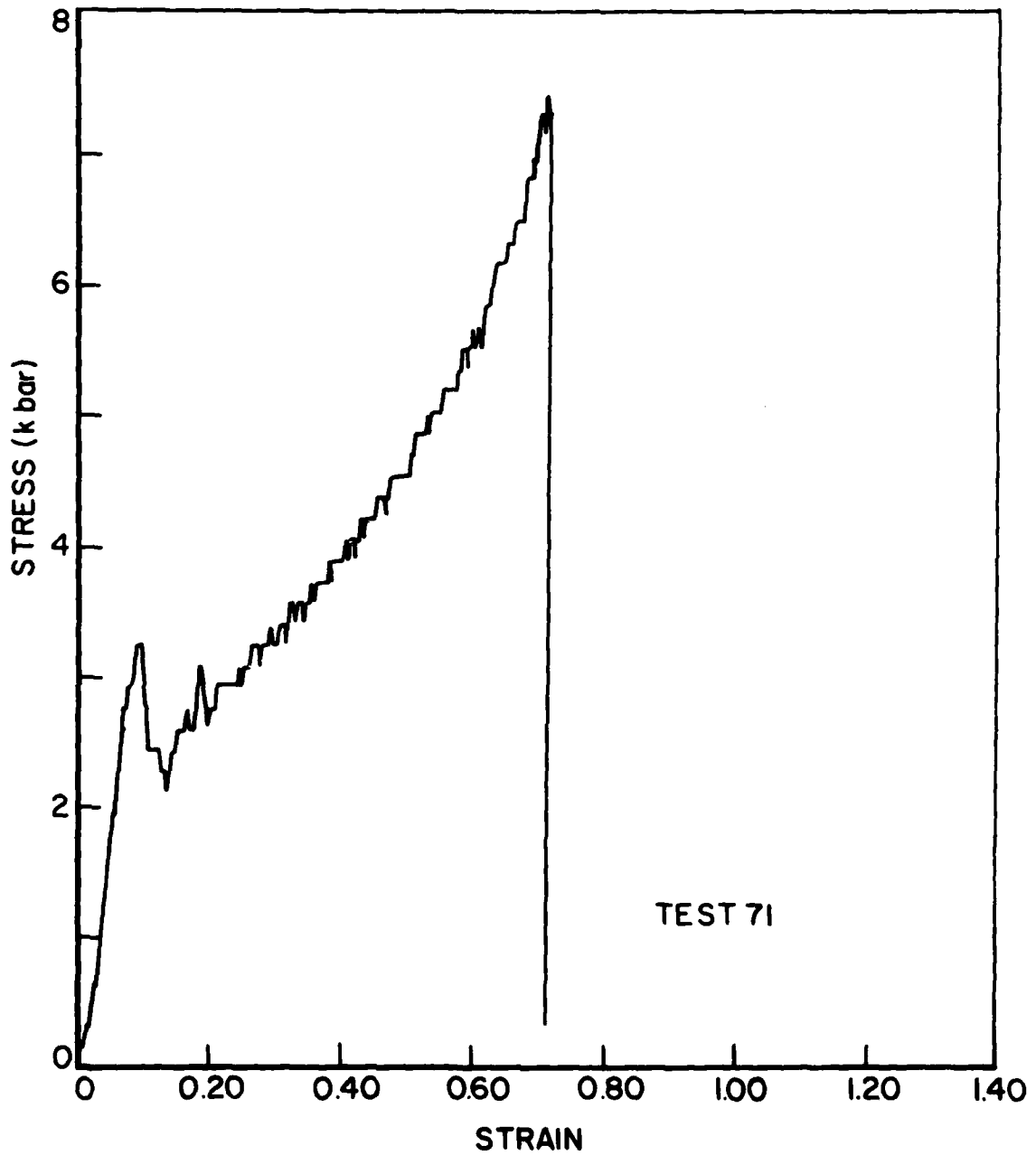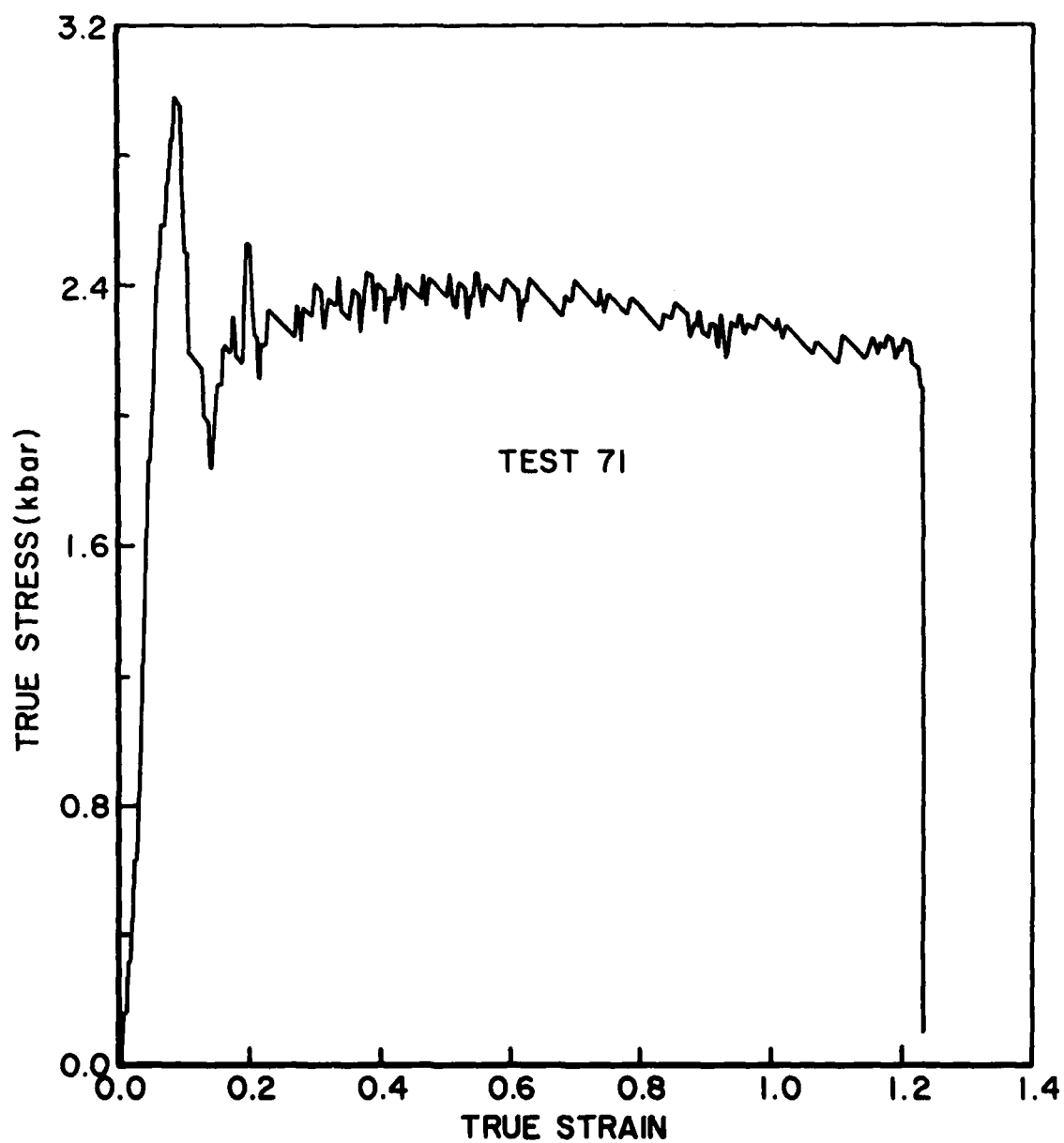
(a)

Figure 28. Compression Test Data for 3003 Aluminum. (a) Stress-strain Curve, (b) Strain Rate, Strain, and Strain as Functions of Time, (c) True Stress-True Strain Curve.

51
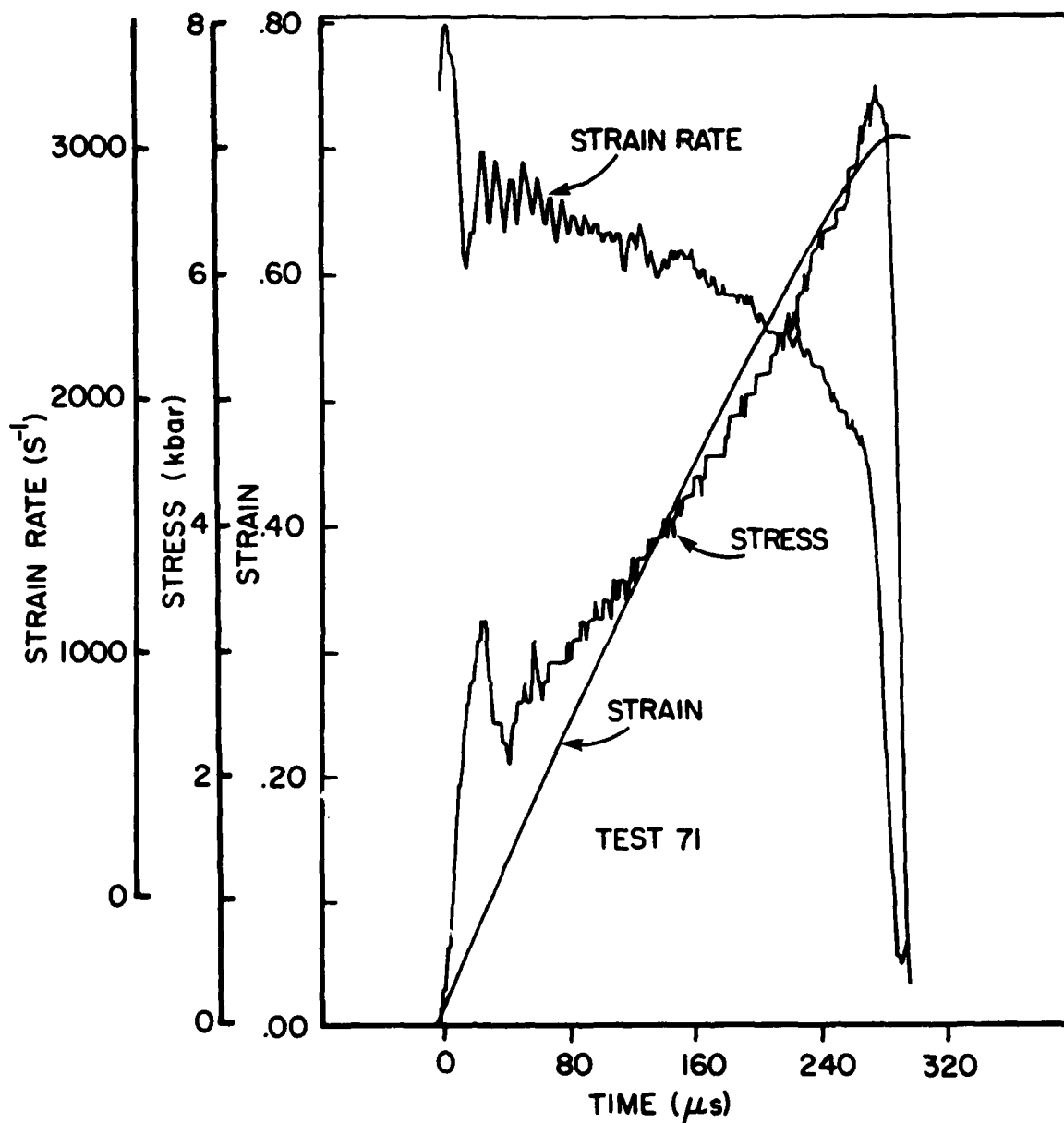
(b)

Figure 28. Compression Test Data for 3003 Aluminum. (a) Stress-strain Curve, (b) Strain Rate, Strain, and Stress as Functions of Time, (c) True Stress-True Strain Curve.
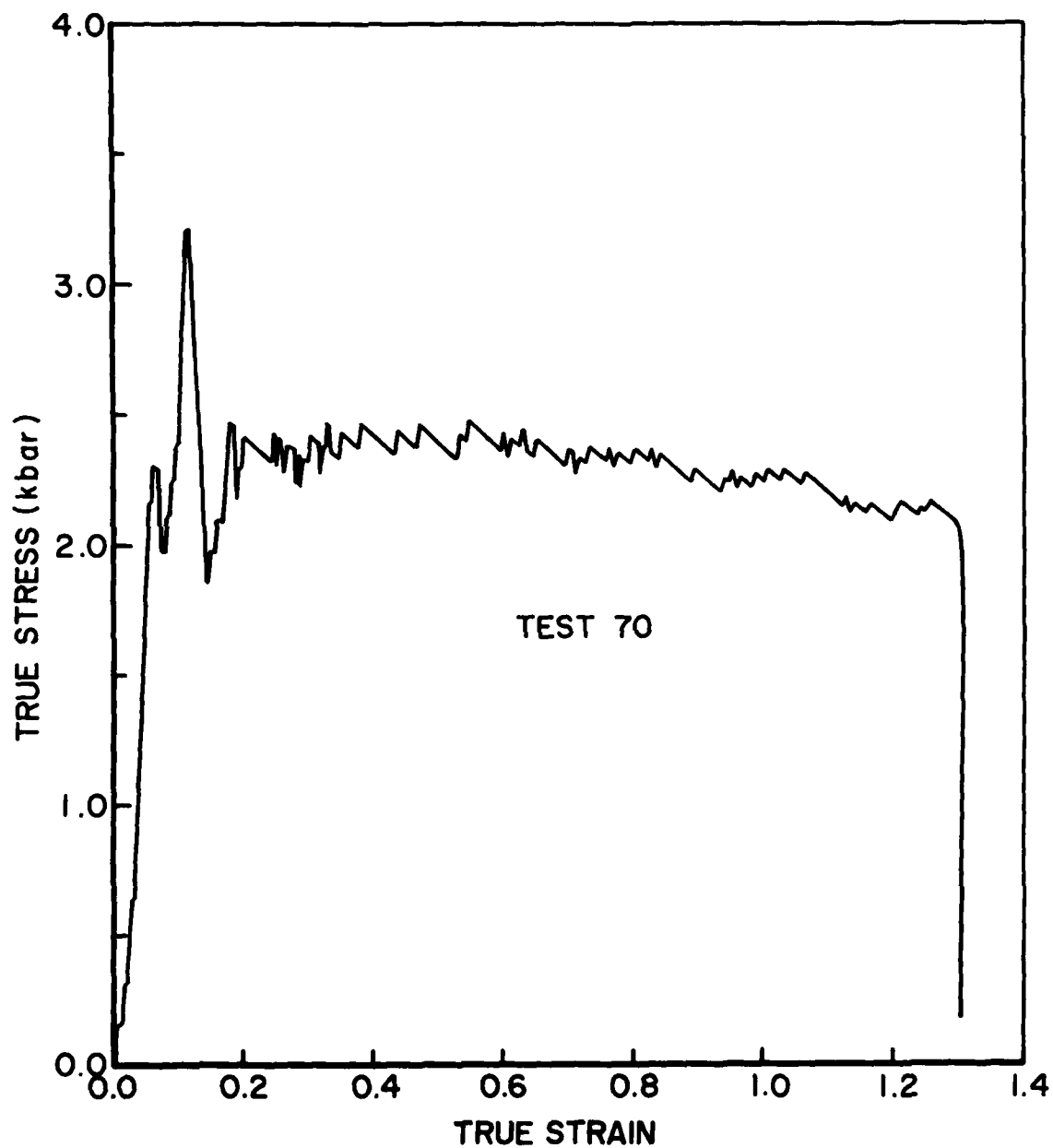
(c)

Figure 28. Compression Test Data for 3003 Aluminum. (a) Stress-
strain Curve, (b) Strain Rate, Strain, and Stress as
Functions of Time, (c) True Stress-True Strain Curve.
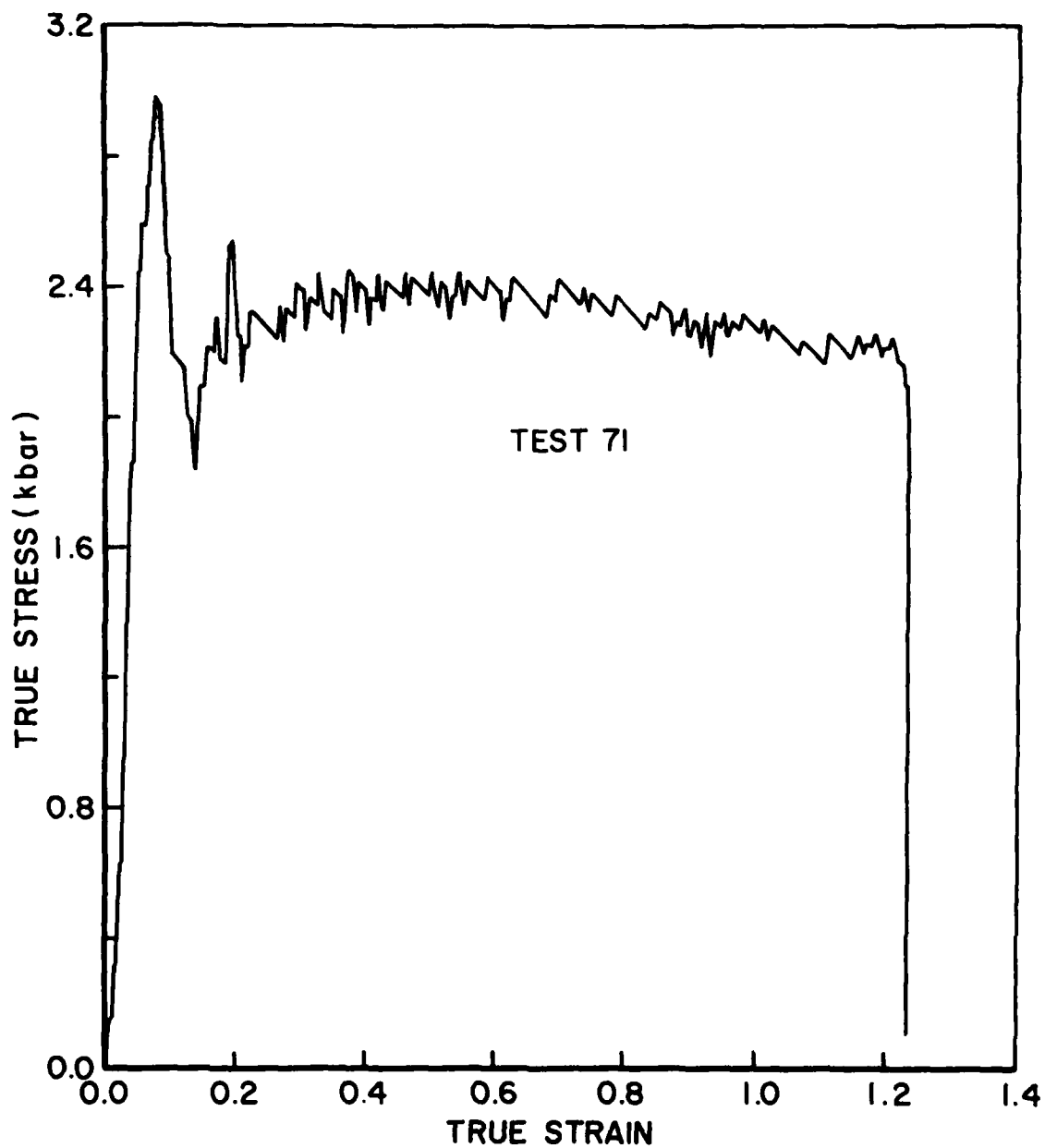
53

Figure 29.   True Stress-True Strain Curve for 3003 Aluminum in
             Compression.   (a) shot 69, (b) shot 70, (c) shot 71.

54
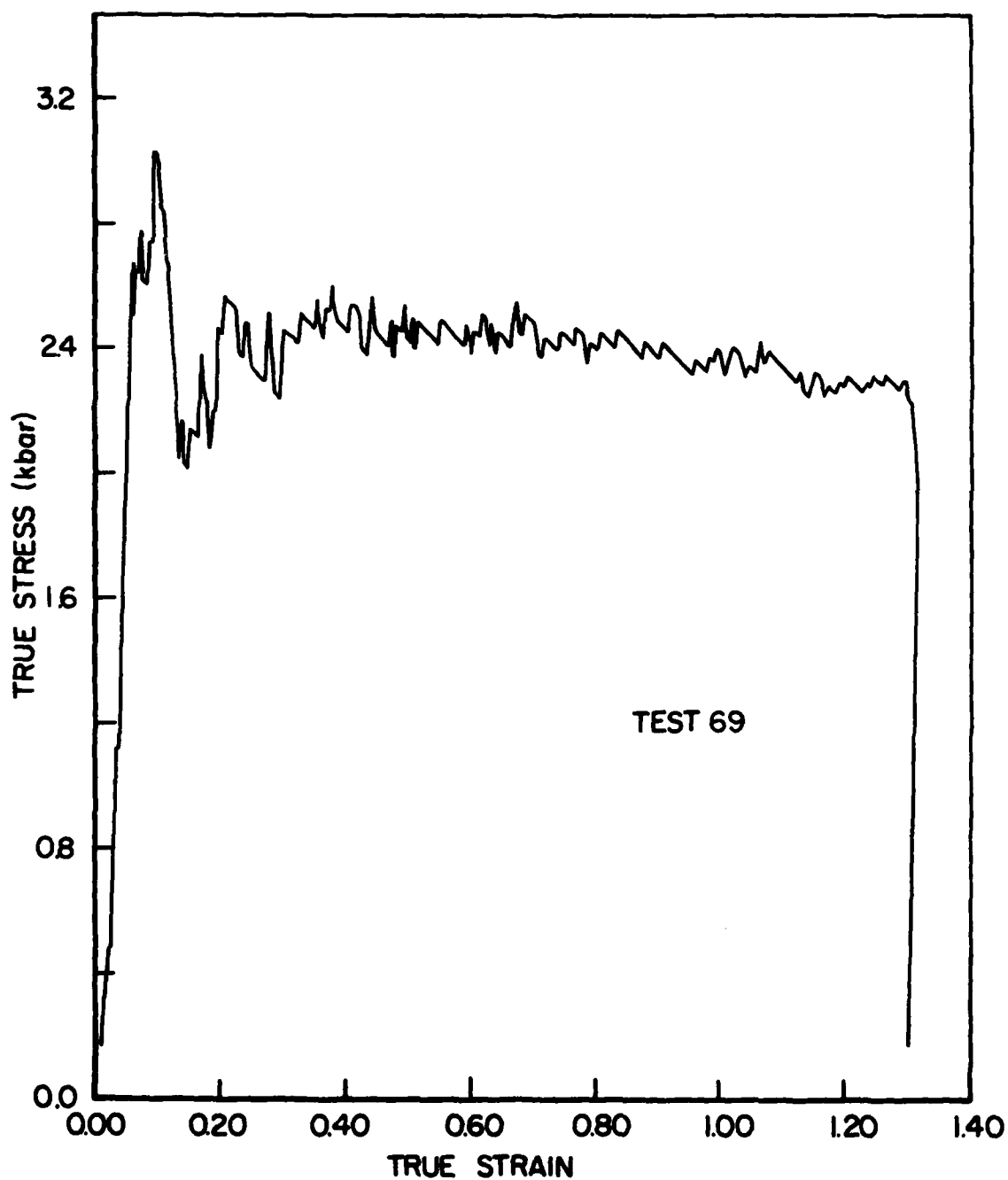
(b)

Figure 29. True Stress-True Strain Curve for 3003 Aluminum in Compression. (a) shot 69, (b) shot 70, (c) shot 71.

Figure 29.   True Stress-True Strain Curve for 3003 Aluminum in
             Compression.   (a) shot 69, (b) shot 70, (c) shot 71.

56

6.2.4 Aluminum 2024-T4 Alloy

Five 2024-T4 aluminum specimens were supplied
by AFATL/DLJW (Eglin Air Force Base). Four were tested dynam-
ically in tension with the Hopkinson Bar apparatus at strain
rates ranging from 280 to 800 s^{-1}, and one was loaded statically
to failure at a 0.001 s^{-1} strain rate. Smoothed stress-strain
curves of this material are presented in Figure 30, and a true
stress-true strain curve from the low rate test is presented
in Figure 31. These stress-strain curves show that this
material is strain rate sensitive. The yield stress increased
with strain rate. They also show that the 2024-T4 strain
hardens at low and moderate ε .rain rates (up to 500 s^{-1}). The
flow stress becomes constant at higher strain rates. Shot
HB050 was particularly interesting; the specimen failed during
the first tensile wave, and the observed stress and strain of
failure were 5.1 kbar and 0.21 respectively.

6.2.5 OFHC Copper

Four annealed OFHC copper specimens supplied by
AFATL/DLJW (Eglin Air Force Base) were tested in tension at
strain rates ranging from 350 to 860 s^{-1}. The individual data
indicated that this material has very low strain rate sensitivity
for the range tested. An average stress-strain curve from these
tests is presented in Figure 32. Similar results were reported
in references 19 and 20. A correction of the data to true
stress reveals that flow stress continuously increases with
strain.

One OFHC copper specimen was machined at the
University and tested in tension at a strain rate of 750 s^{-1}.
A smoothed stress-strain curve from this test is presented in
Figure 33. The yield stress of this specimen was considerably
higher than the yield stress, observed at similar strain rates,
of the annealed OFHC supplied by AFATL/DLJW. This discrepancy
is attributed to the cold work effects. The specimen was not

annealed after machining. This interpretation agrees with
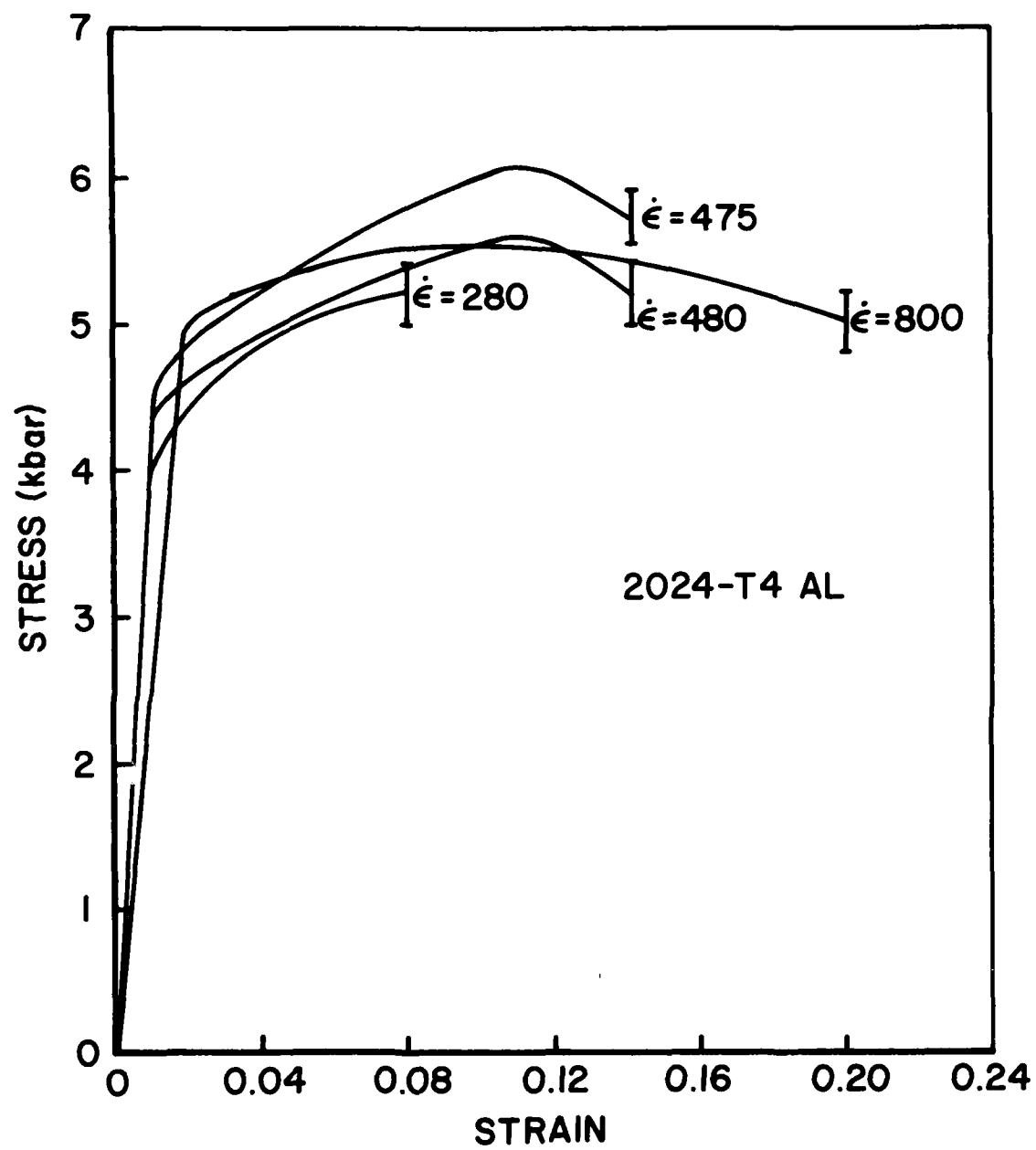the effects of cold work that was reported in reference
20.

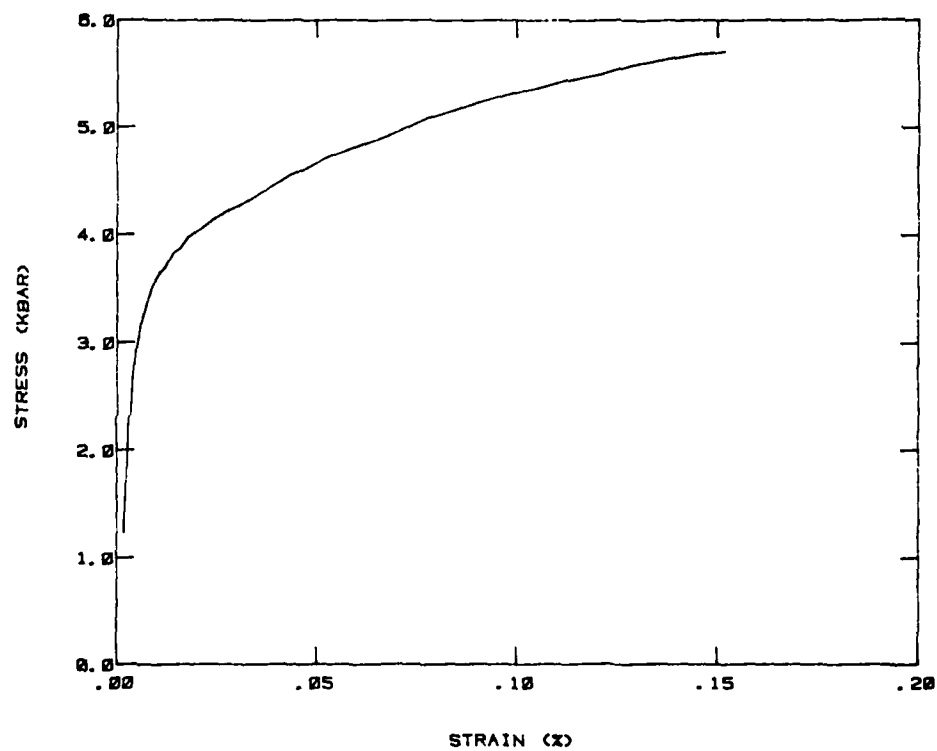Figure 30. Stress-strain Behavior of 2024-T4 Aluminum at Various Strain Rates.

Figure 31.   True Stress versus True Strain for 2024-T3 Aluminum
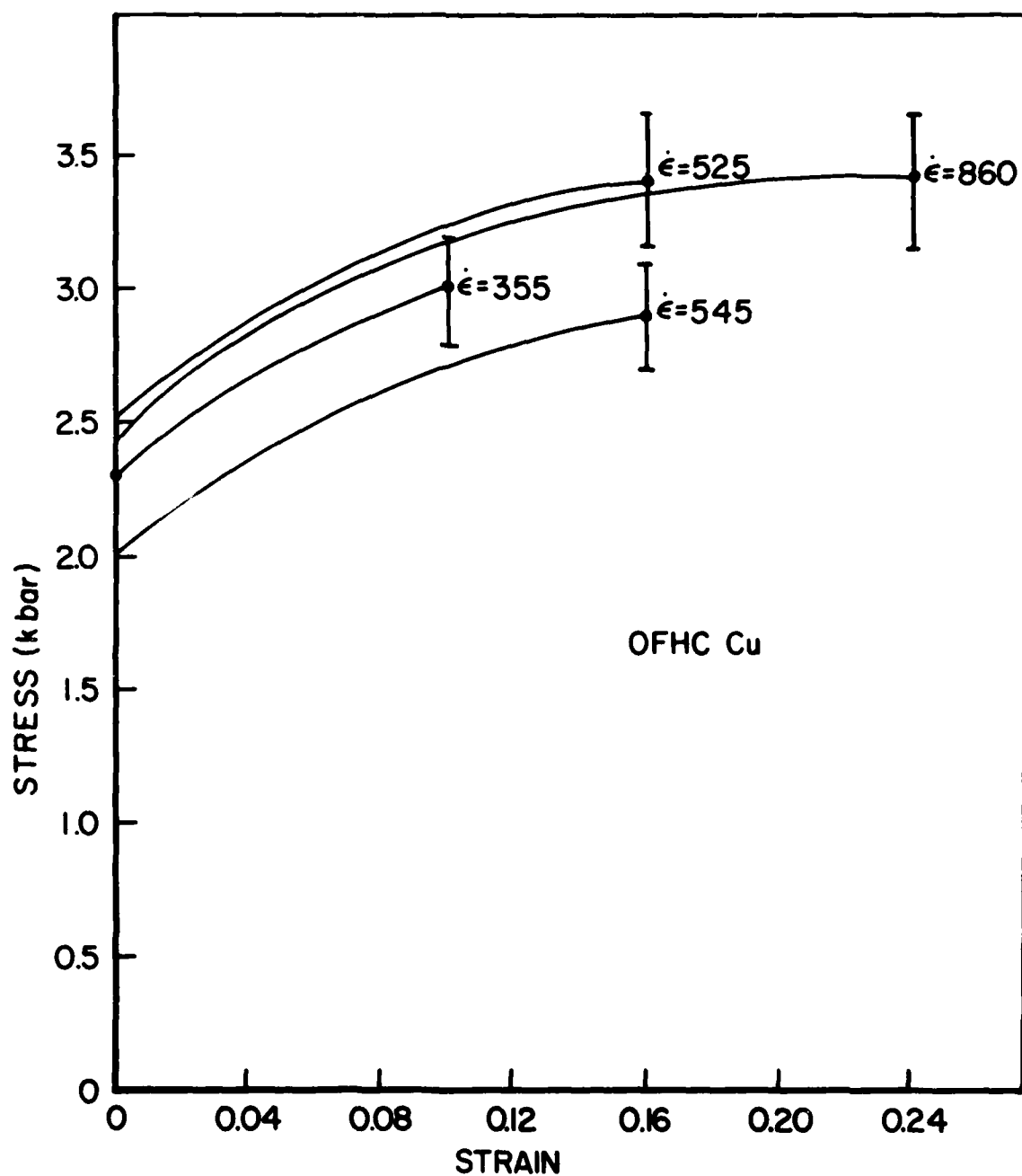   for $\dot{\epsilon} = 10^{-3}$.

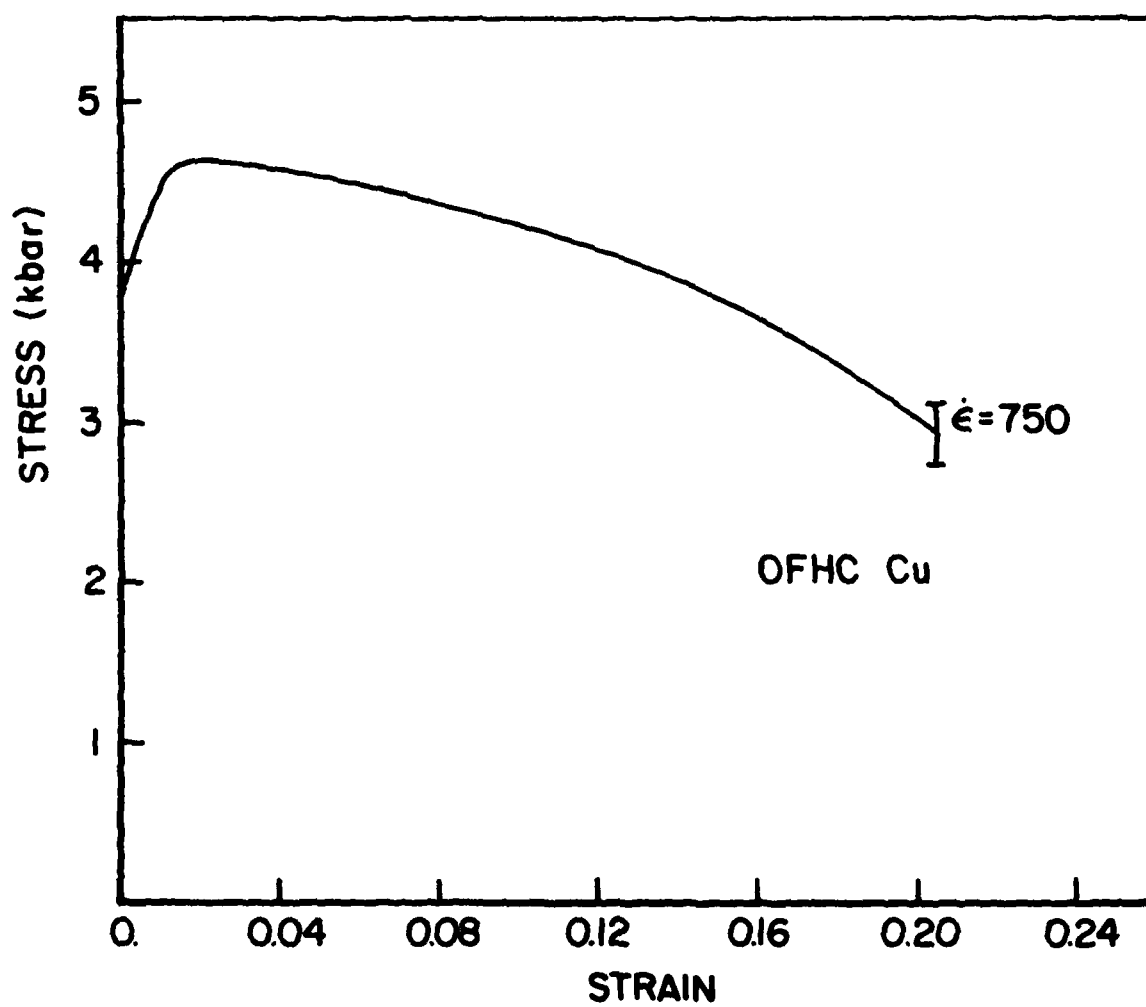Figure 32.   Stress-strain Behavior of Annealed OFHC Copper.

61

Figure 33. Stress-strain Behavior of Worked OFHC Copper.

REFERENCES

1.   National Materials Advisory Board, "Material Response to Ultra-High Loading Rates," PB80-15352, 1980.

2.   Bless, S. J. and J. P. Barber, "Impact Induced Tesnile Failures in Steel," AFML-TR-79-4020, February 1979.

3.   Bless, S. J., "Spall Criteria for Several Metals," AFWAL-TR-81-4040, June 1981.

4.   Seaman, L., T. W. Barber, and D. R. Curran, "Dynamic Fracture Criteria of Homogeneous Materials," AFWL-TR-71-156, February 1972.

5.   Barker, L. M. and R. E. Hollenbach, "Shock Wave Study of $\alpha \rightarrow \epsilon$ Phase Transition in Iron," _J. Appl. Phys._, _45_, 4872-87, 1974.

6.   Barker, L. M. and R. E. Hollenbach, "Shock Wave Studies of PMMA, Fused Silica, and Sapphire," _J. Appl. Phys._, _41_, 4208-4226, 1970.

7.   Chhabildas, L., private communication, 1981.

8.   Hauver, G. E., "The Alpha-phase Hugoniot of Rolled Homogeneous Armor," ADB012871, August 1976.

9.   Shockey, D. A., et al., "A Computational Model for Fragmentation of Armor Under Ballistic Impact," ADB004672, April 1975.

10. Christman, D. R. and W. M. Isbell, "Measurements of Dynamic Properties of Materials V, OFHC Copper," AD728 864, July 1971.

11. Bauer, D. P. and S. J. Bless, "Strain Rate Effects on Ultimate Strain of Copper," AFML-TR-79-4021, November 1978.

12. Forrestal, M. J., B. W. Duggin, and R. I. Butler, "An Explosive Loading Technique for the Uniform Expansion of 304 Stainless Steel Rings at High Strain Rates," _J. Appl. Mech._, _47_, 17-20, 1980.

13. Wesenberg, D. L. and M. J. Sagartz, "Dynamic Fracture of 6061-T6 Aluminum Cylinders," _J. Appl. Mech._, 44, 643-646, 1977.

14. Fyfe, I. M. and A. M. Rajendran, "Dynamic Pre-strain and Inertia Effects on the Fracture of Metals," _J. Mech. Phys. Solids_, _28_, 1980.

15. Warnes, R. H., et al., "An Improved Technique for Determining Dynamic Material Properties Using the Expanding Ring," in Shock Waves and High-Strain-Rate Phenomena in Metals, ed. M. A. Meyers and L. E. Munrr, Plenum Press, 1981.

16. Kury, J. W., H. C. Hornig, E. L. Lee, J. L. McDonel, D. L. Ornellas, M. Finger, F. M. Strange, and M. L. Wilkins, "Metal Acceleration by Chemical Explosive," Fourth International Symposium on Detonation, AD 656035, pp 3-11, 1966.

17. Nicholas, T., "Dynamic Tensile Testing of Structural Materials Using a Split Hopkinson Bar," AFWAL-TR-80-4053, October 1980.

18. Manjoine, M. J., "Influence of Rate of Strain and Temperature on Yield Stresses of Mild Steel," Journal of Applied Mechanics (1944).

19. Lindholm, U. S. and R. L. Bessey, "A Survey of Rate Dependent Strength Properties of Metals," AFML-TR-69-119, April 1969.

20. Green, S. J., C. J. Maiden, S. G. Babcock, and F. L. Schlierloh, "The High Strain-Rate Behavior of Face-Centered Cubic Metals," General Motors Technical Center.

21. Hutchinson, J. W. and K. W. Neale, Acta Metall. 25, 839, 1977.

22. Ghosh, A. K., Acta Metall. 25, 1913, 1977.

23. Campbell, J. D., et al., Fundamental Aspects of Structural Alloy Design (ed. R. J. Jafu), p. 545, Plenum Press, NY, 1977.

24. Sagat, S. and D. M. R. Taplin, Metal Sci. 10, 94, 1976.